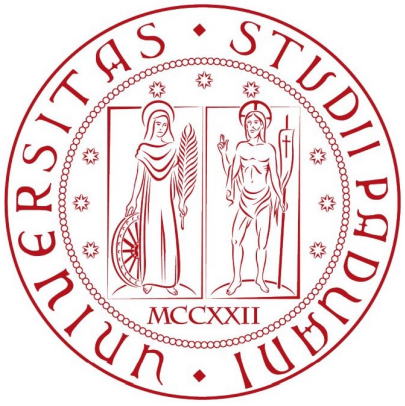

UNIVERSITÀ DEGLI STUDI DI PADOVA

Dipartimento di Fisica e Astronomia

Corso di Laurea Triennale in Astronomia

Perseus Galaxy cluster's magnetic field at the position of the radio galaxy IC310 for ALP searches with Cherenkov telescopes

Relatore:
Prof. Michele Doro

Correlatore:
Dott.ssa Ivana Batkovic
Prof. Alessandro De Angelis

Candidato:
Jean-Pierre Jonckheere

ANNO ACCADEMICO 2021/2022

Contents

List of Figures

Executive Summary

Magnetic fields in the intracluster medium have been measured over the past decades using a variety of techniques, including searches for synchrotron relic and halo radio sources within clusters, studies of inverse Compton X-ray emission from clusters, surveys of Faraday rotation measures of polarized radio sources both within and behind clusters, and studies of cluster cold fronts in X-ray images. These measurements imply that most cluster atmospheres are substantially magnetized. The importance of these magnetic fields is utmost; they are fundamental for understanding the physical and the energetical conditions of the ICM. In this thesis, we investigate the magnetic field in the Perseus cluster discussing the current knowledge about its value in the cluster core and at the position of IC310, a galaxy in the outer region of cluster. We have found evidence that the magnetic field in IC310 must be $\geq 1\mu$ G. The aim of this study is to use this result to place constraints on the research of axion-like particles, with ground based Cherenkov telescopes, using irregularities in the high-energy spectra of astrophysical sources, imprinted by such exotic particles.

Sommario

I campi magnetici nel mezzo intracluster sono stati misurati negli ultimi decenni utilizzando una diverse tecniche, basate su ricerch synchrotron relics e sorgenti di halo radio all'interno di cluster, indagini sull'emissione in X per effetto Compton inverso dai cluster, analisi sulle misure di rotazione di Faraday di sorgenti radio polarizzate sia internamente che esternamente al cluster e studi sui fronti freddi dei cluster nelle immagini in X. Queste misurazioni implicano che la maggior parte delle atmosfere dei cluster sono sostanzialmente magnetizzate. L'importanza di questi campi magnetici è massima, sono fondamentali per comprendere le condizioni fisiche ed energetiche dell'ICM. In questa tesi, abbiamo investigato il campo magnetico del Cluster Perseus, discutendo la attuale conoscenza sul suo valore nel cluster core e nella posizione di IC310. Si è trovata evidenza che il campo magnetico in IC310 è necessariamente ≥ 1 μG. Lo scopo di questo studio è applicare i risultati per la ricerca delle particelle Axion-like, tramite telescopi Cherenkov a terra, usando la mancanza di irregolarità in sorgenti astrofisiche di alta energia, dovuta a queste particelle esotiche.

Introduction

Most of the matter in the Universe is composed of ionized or partially ionized gas permeated by magnetic fields. These magnetic fields play an important role in virtually all astrophysical phenomena. Celestial objects are magnetized and have magnetic fields of significant strength. Such fields are found everywhere in the interstellar space and over both small and large scales in the extragalactic universe. In general, small, compact objects have the largest magnetic field strengths, while larger, low-density objects, or structures have weaker magnetic fields.

On Earth, we have a bipolar magnetic field with a strength of 0.3 G at the equator and 0.6 G at the poles. It is thought that this field originates in a dynamo from the circular motion of a charged fluid inside the molten metallic core (Soward 1983). A similar mechanism produces the solar magnetic field. This field has a strength of 10 G at the poles and gives rise to spectacular sunspots, arches, and flares (Parker 1979). Within the interstellar medium, magnetic fields are thought to regulate star formation via the ambipolar diffusion mechanism (Spitzer 1978). Our own Galaxy has a typical interstellar magnetic field strength of $\sim$ 2-5 μG. It is characterized by a spiral shape, it is present in the Galaxy in a regular ordered component on kpc scale, and has a similar value in a smaller scale, random component (Beck 1996; Kulsrud 1999). Other spiral galaxies have been estimated to have magnetic field strengths of 5 to 10 μG on average, with values up to $\sim$ 30 μG in massive spiral arms and $\sim$ 50μG in starburst galaxies (Beck 1996). Magnetic fields of the order of $\sim \mu$G are fundamental to the observed properties of jets and lobes in radio galaxies (Bridle 1984).

The newest area of study of cosmic magnetic fields is on even larger scales, those of clusters of galaxies. Galaxy clusters are the largest virialized structures observed in the Universe. The study of cluster magnetic fields is important to understand the physical conditions and the balance of energy of the intracluster medium. Cluster magnetic fields provide an additional term of pressure and may play a role in the cluster dynamics. They couple cosmic ray particles to intracluster gas and they can inhibit transport processes like heat conduction, spatial mixing of gas, and propagation of cosmic rays. They are essential for the acceleration of cosmic rays and make it possible to observe the cosmic ray electron population by the synchrotron radiation. These large-scale magnetic fields could also be the key to understand the photon/ALP mixing. Pseudoscalar Axion-Like particles (ALP) are common in various extensions of the Standard Model of particle physics (Jaeckel 2010). Their defining property is the interaction with the electromagnetic field, allowing for photon-ALP mixing in an external magnetic field (Raffelt and Stodolsky 1988). Experimentally, the allowed values of the mass are very low, $m_{ALP} \sim 10^{-7} - 10^{-9}$ eV. This makes large-scale astrophysical environments the best place to search for manifestations of this interaction. Photon-ALP mixing may result in oscillatory features in the spectra of astrophysical sources of gamma rays seen through regions filled with magnetic fields. While the precise shape of these irregularities and the photon energies at which they appear depends on the ALP parameters (mass, cross section) and magnetic field configurations, these features are not expected in the otherwise smooth astrophysical spectra. The lack of these irregularities in the observed spectra might in principle be used to constrain ALP parameters. In this discussion we will firstly introduce the fundamentals of what a Cluster of Galaxies is, then we will proceed to summarize and discuss the known methods for measuring the cluster magnetic field. We will then synthesize the basic theory behind ALP's. To conclude we will try to apply this knowledge to the Perseus Cluster to have a general picture of its magnetic field.

1. Clusters of Galaxies

1.1 Basis of Cluster of Galaxies

Cluster of galaxies, or Galaxy Cluster (GC), are among the largest gravitationally bounded systems in the Universe, believed to be the largest known structures in the universe until **superclusters** were discovered. A cluster is a structure that consists of hundreds to thousands of galaxies that are bound together by gravity, having a typical mass range of $10^{14} - 10^{15}$ $M_{\odot}$[1] and typical diameter extension of 1-5 Mpc. In the observable universe it is supposed that around 10 million clusters exist. Some of the most famous clusters are:

- Virgo Cluster: closest one to us being the Virgo Cluster (∼16.5-18 Mpc from earth);
- Bullet Cluster: a cluster merger with the first observed separation between dark matter and normal matter;
- Perseus cluster: is the brightest cluster in the sky when observed in the X-ray band, subject of our studies;
- CL J1001+0220: most distant cluster at z = 2506;
- Pandora Cluster: named because the cluster resulted from a collision of clusters, which resulted in many different and strange phenomena.

More can be found in the Catalogue of Galaxies and of Clusters of Galaxies written by Fritz Zwicky[2]. They appear at optical wavelengths as over-densities of galaxies with respect to the field average density of the medium. In the hierarchical scenario of structure formation, clusters of galaxies are formed by the gravitational merger of smaller units, e.g., groups and subclusters (Govoni 2018). Such mergers are spectacular events that involve kinetic energies as large as $\simeq 10^{64}$ erg. In these mergers, a large portion of the energy is dissipated in the Intracluster medium, generating shocks, turbulences and bulk motions, thus heating it. The substructures in the X-ray images as well as complex gas temperature gradients are signatures of cluster mergers The intracluster medium, usually denoted by the acronym **ICM**, is a hot ($T \simeq 10^8$ K) and low electronic density gas ($n_e \simeq 10^{-3}$ cm^{-3}). The detection is through its luminous X-ray emission ($L_X \simeq 10^{43} - 10^{45}$ erg·s^{-1}), produced by **thermal bremsstrahlung** radiation (Govoni 2018).

Different models have been proposed to explain the origin and emission of this electrons (Carilli 2002):

- primary electron models in which relativistic electrons are injected in the ICM from AGN[3] activity (quasar, radio galaxies, etc.) and/or from star formation in galaxies (supernovae, galactic winds, etc.). The radiative lifetime of relativistic electrons is relatively short ($\sim 10^{7-8}$ yrs). Therefore, models involving a primary origin of the relativistic electrons require continuous injection processes and/or re-acceleration processes to explain the presence of diffuse non-thermal emission out to Mpc scales. Electrons are likely re-accelerated in the gas turbulence or in shocks, although the efficiency of the latter process is debated.

[1] $M_{\odot}$ means solar mass as a unit of measure.
[2] https://authors.library.caltech.edu/37997/
[3] Active Galactic Nucleus.

- Secondary electron models in which cosmic ray electrons result as secondary products of hadronic collisions between relativistic protons and ICM thermal protons. Relativistic protons in the ICM have lifetimes of the order of Hubble time[4]. Thus, they are able to travel a long distance from their source before they release their energy. In this way, electrons are produced through the whole cluster volume and do not need to be re-accelerated. The production of relativistic electrons by secondary models predicts large gamma-ray fluxes from neutral pion decay, which could be tested by future gamma-ray missions.

[4]The time required for the Universe to expand to its present size.

1.2 Detection

Visible galaxies and the ICM are important components of clusters, however, most of the cluster's mass (up to 85-90%) is in **dark matter** (DM). The name is due to of its lack of interaction with the electromagnetic field and because it appears obscure and invisible. Although DM has not been directly observed at any wavelength and its nature remains unknown, it has been inferred through gravitational interactions. X-ray and visible light observations provide clues to its amount and distribution in clusters. X-ray images, such as the ones obtained with ROSAT[5], ASCA[6], Chandra[7] and XMM-Newton[8], provide a powerful technique for tracing the gravitational potential of clusters and for probing the dynamics, morphology, and history of clusters.

The physics of the ICM and inside is still a subject of debate. For example, a significant fraction of clusters of galaxies show the X-ray surface brightness strongly peaked at the center. This implies a high density and large cooling time of the hot ICM within the inner, $\simeq$100 kpc, much shorter than the Hubble time (Carilli 2002). The cooling time drops further at smaller radii, this suggest that in absence of any balancing heat source much of the gas is cooling out of the hot ICM. X-ray observations with XMM-Newton indicate that there is no spectral evidence for large amounts of cooling and condensing gas in the centers of galaxy clusters where it is believed to harbor strong cooling flows. The cooling flow seems to be hindered by some mechanism whose nature is still extensively discussed. Therefore, there is no consensus on the actual existence of material *cooling* and *flowing*. What is generally agreed upon is that cooling core clusters are more dynamically relaxed than non-cooling core clusters, which often show evidence of cluster merger (Govoni 2018; Carilli 2002).

One of the most important results obtained with the Chandra satellite on clusters of galaxies was the discovery of sharp surface brightness discontinuities in the images of merging clusters, called **cold fronts** (for more on this subject see sec. 2.8). Initially, one might have suspected these features to be merger shocks, but spectral measurements showed that these are a new kind of structure. These cold fronts are apparently contact discontinuities between the gas, which was in the cool core of one of the merging sub-clusters, and the surrounding intracluster gas. Cold fronts and merger shocks offer unique insights into the cluster physics, including the determination of the gas bulk velocity, its acceleration, the growth of plasma instability, the strength and structure of magnetic fields, and the thermal conductivity (Govoni 2018; Carilli 2002). Even if most emissions for GC is emitted in X-ray trough thermal bremsstrahlung some clusters of galaxies are also known to have diffuse sources of radio emission which cannot be attributed to single galaxies in the cluster. The main properties of radio sources were derived from a few clusters where clear identification and distinction from other cluster radio sources have been made. Halo sources appear to have steep spectral index, i.e, the radio flux drops with increasing frequency ν with a power larger than -1, typically as $\nu^{-1.2}$, a moderately high radio luminosity, i.e., about 10^{31}-10^{32} erg s^{-1} Hz^{-1} at a wavelength and large size but localized size (diameter of about 1 Mpc) (see sec. 2.2.1, 2.2.3, 2.2.2).

[5]German Aerospace Center-led satellite X-ray telescope.

[6]Advanced Satellite for Cosmology and Astrophysics, Japan's fourth cosmic X-ray astronomy mission.

[7]NASA's telescope specially designed to detect X-ray emission from very hot regions of the Universe.

[8]ESA's X-ray space observatory.

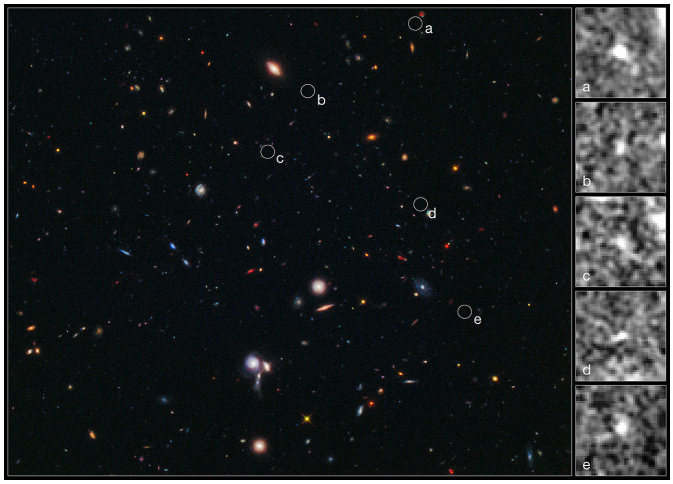

Figure 1.1: Composite image of five galaxies clustered together just 600 million years after the Universe's birth.

Figure 1.2: Deep Field photo of the Galaxy cluster SMACS J0723.3-7327 taken by the James Webb Space telescope (JWST).

2. Theoretical Background Related to Cluster Magnetic Fields

In this section we are going to show the theoretical basis of Cluster Magnetic Fields as an introduction to the work performed in this thesis.

2.1 Magnetic Field in Cluster of Galaxies

Nowadays we know that most of the matter in the Universe is composed of ionized, or partially ionized, gas permeated by magnetic fields. Despite there being done several observational efforts to measure their properties, our knowledge on cluster magnetic fields is still poor. Normally, small compact astronomical objects have the largest magnetic field strengths, while larger low-density objects have weaker magnetic fields. For object like GCs, a magnetic field strength of the order of $\sim \mu$G is expected due to their large scale (Govoni 2018). Magnetic fields in the ICM have been measured using several techniques: studies of *synchrotron relic* and *halo radio sources* within clusters, studies of *inverse Compton X-ray emission* from clusters, surveys of *Faraday rotation measures* of polarized radio sources both within and behind clusters, and studies of cluster *cold fronts* in X-ray images.

2.1.1 Non-thermal phenomena related to the Magnetic Field

The magnetic field has important dynamical effects, however, it is very difficult to measure. The synchrotron emission of the source and the Faraday effect are the only direct observable effects. Faraday rotation measurements of radio sources in clusters indicate that the general cluster magnetic field is probably highly tangled. The best-studied GC so far is the Coma cluster. The limits found on the field strength in Coma range from about 0.3 μG, set by upper limits on the IC X-radiation from the cluster, to about 10 μG (Jaffe 1980).

An ICM physical description also necessitates precise knowledge of non-thermal components. The most detailed evidence for these phenomena comes from radio observations. A number of clusters of galaxies are known to contain diffuse synchrotron sources, e.g, radio halos, relics, and mini-halos, which have no connection with the cluster's galaxies, but are rather associated with the ICM. Synchrotron emission from such sources requires a population of $\sim$ GeV relativistic electrons and cluster magnetic fields on μG levels. The indirect evidence for the existence of cluster magnetic fields is also derived from studies of the **Rotation Measure** (RM) of radio galaxies located within or behind clusters of galaxies. A probe of the existence of a population of relativistic electrons in the ICM is also obtained from the detection of non-thermal emission of **inverse Compton** (IC) origin in the hard X-ray and possibly in the extreme ultraviolet wavelengths (Carilli 2002; Govoni 2018).
The combination of the observed diffuse radio and hard X-ray emissions from clusters of galaxies is used to estimate the intracluster magnetic field strength.

2.2 Synchrotron Radiation

Synchrotron emission, also known in literature as *magnetobremsstrahlung radiation*, is produced by the spiraling motion of relativistic electrons in a magnetic field when the relativistic charged particles are subject to a centripetal acceleration perpendicular to their velocity ($a \perp v$). The radiation produced has a characteristic polarization and the frequencies generated can range over a large portion of the electromagnetic spectrum. Therefore, detecting synchrotron emission is a direct way to detect magnetic fields in astrophysical sources. The total synchrotron emission from a source provides an estimate of the strength of magnetic fields, at the same time the degree of polarization is an important indicator of the field uniformity and structure. The energy of an electron under relativistic conditions is given by:

$$E = \gamma m_{\mathrm{e}} c^2 \tag{2.1}$$

where γ is the Lorentz factor. In a magnetic field we recall that the trajectory of the electron follows the field lines in a elicoidal motion because it is subject to the Lorentz force.

$$F_{\mathrm{L}} = q \cdot (v \times B). \tag{2.2}$$

The relativistic gyrofrequency is:

$$\nu_g = \gamma^{-1} \frac{eB}{2\pi m_{\mathrm{e}} c} \tag{2.3}$$

γ=1 gives the classical value for ν_g.

In the astrophysical studies of cosmic ray, usually very high values of $\gamma \sim 10^3 - 10^5$ are taken, so one would suggest that synchrontron radiation should have a very low frequency, even lower than classical results, so low that it might be difficult to observe. However, what is observed is a very high frequency, even higher than what can be calculated with the formula above. The reason for this is that in the relativistic regime the emission is perpendicular to the acceleration vector in a cone that has for the axis the instantaneous velocity vector and half-angle inversely proportional to its energy ($\propto \gamma^{-1}$).
To the observer, the radiation is essentially a continuum with a fairly peaked spectrum concentrated near the critical frequency:

$$\nu_{\mathrm{c}} = c_1 B \sin\theta E^2. \tag{2.4}$$

The synchrotron power emitted by a relativistic electron is

$$-\frac{d\varepsilon}{dt} = c_2 (B \sin\theta)^2 E^2 \tag{2.5}$$

where θ is the pitch angle between the velocity of the electron and the direction of the magnetic field, while c_1 and c_2 depend only on fundamental physical constants:

$$c_1 = \frac{3e}{4\pi {m_{\mathrm{e}}}^3 c^5}, \qquad c_2 = \frac{2e^4}{3{m_{\mathrm{e}}}^4 c^7}. \tag{2.6}$$

Therefore, at a given frequency, the energy, or Lorentz factor, of the emitting electrons depends directly on the magnetic field strength. The higher the magnetic field strength, the lower the electron energy needed to produce emission at a given frequency.

2.2.1 Radio Halos

Radio halos typically have sizes ~ 1 Mpc, steep spectral indices $\alpha > 1$, low fractional polarizations $< 5\%$, low surface brightnesses $\sim 10^{-6}$ Jy $\cdot$arcsec^{-2} at 1.4 GHz, and centroids close to the center of the cluster defined by X-ray emission. On the observational side, it is possible to draw some of the general characteristics of radio halos and derive correlations with other cluster properties:

- halos are typically found in clusters with significant substructure and deviation from spherical symmetry in X-ray morphology. This is confirmed by the high-resolution X-ray data obtained with Chandra and XMM. In addition to the distorted X-ray morphology, all of the halos exhibit strong gas temperature gradients. Some clusters show a spatial correlation between the radio halo brightness and the hot gas regions, although this is not a general feature;

- in a number of well-resolved clusters, a point-to-point spatial correlation is observed between the radio brightness of the halo and the X-ray brightness as detected by ROSAT. This correlation is visible, e.g., in the Chandra high resolution data;

- halos are present in rich clusters, characterized by high X-ray luminosity and temperature. The percentage of clusters with halos in a complete X-ray flux-limited sample, which includes systems with $L_X > 5 \times 10^{44} {h^{-2}}_{50}$ erg$\cdot$s^{-1} in the $0.1 - 2.4$ keV band, is $\simeq 5\%$. The halo fraction increases with the X-ray luminosity to $\simeq 33\%$ for clusters with $L_X > 10^{45} {h^{-2}}_{50}$ erg$\cdot$s^{-1};

- the radio power of a halo strongly correlates with the cluster luminosity, gas temperature and the total mass.

In 1959 studies (Large 1959), an extended radio source was discovered in the Coma cluster, it could be observed with a 45' beam. A few years later, in 1970, Coma C was studied (Willson 1970), who found that it had a steep spectral index and could not be made up of discrete sources but instead was a smooth *radio halo* with no structure on scales smaller than 30'. Willson assumed that the emission mechanism was likely to be synchrotron and the equipment required a magnetic field strength of 2 μG.

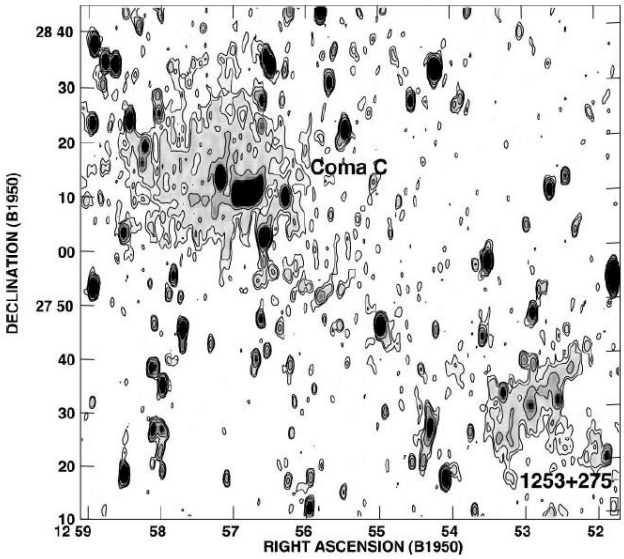

Figure 2.1: Westerbork Synthesis Radio Telescope (WSRT) radio image of the Coma cluster region at 90 cm, with angular resolution of 55" × 125" (HPBW, $RA \times DEC$) for the radio telescope. Labels refer to the halo source Coma C and the relic source 1253 + 275. The gray-scale range displays total intensity emission from 2 to 30 mJy/beam, whereas contour levels are drawn at 3, 5, 10, 30, and 50 mJy/beam. The bridge of radio emission connecting Coma C to 1253 + 275 is resolved and visible only as a region with an apparent higher positive noise. The Coma cluster is at a redshift of 0.023, such that $1' = 26$ kpc for H $_0$ = 75 (Carilli 2002).

Subsequently, other radio halos were discovered. The number of known halos remained low until the work made by Hanisch in 1982 (Hanisch 1970), using the Northern VLA Sky Survey[1], and X-ray selected samples as starting points; deep VLA observations have more than doubled the number of known radio halo sources. Several new radio halos have also been identified from the Westerbork Northern Sky Survey[2].

A steep correlation between cluster X-ray and radio halo luminosity has been found, as well as a correlation between radio and X-ray surface brightnesses in clusters. A complete flux-limited sample of X-ray clusters shows that only 5% to 9% of the sources are detected at the surface brightness limits of the NVSS[3] of 2.3 mJy $\cdot$ beam^{-1} , where the beam has $FWHM$[4] = 45". However, this sample contains mainly clusters with luminosity X-ray $< 10^{45}$ erg $\cdot$s^{-1}. If one selects clusters with X-ray luminosity $> 10^{45}$ erg $\cdot$ s^{-1}, the radio detection rate increases to 35% . There may be a correlation between the existence of a cluster radio halo and the existence of a substructure in X-ray images of the hot cluster atmosphere, indicative of merging clusters, and a corresponding anticorrelation between cluster radio halos and clusters with relaxed morphologies, e.g., cooling flows, although these correlations are just beginning to be quantified. Magnetic fields in cluster radio halos can be derived, assuming a minimum energy configuration for the summed energy of relativistic particles and magnetic fields, corresponding roughly to

[1] astronomical survey of the Northern Hemisphere carried out by the Very Large Array (VLA) of the National Radio Astronomy Observatory (NRAO).

[2] low-frequency radio survey that covers the whole sky north of declination +30.

[3] NRAO VLA Sky Survey.

[4] Full width half maximum.

the energy equipartition between the field and particles. The equations for deriving minimum-energy fields from radio observations are given in (Miley 1980). Estimates for the minimum energy magnetic field strength in cluster halos range from 0.1 to 1 μG (Feretti et al. 1999) . A minimum energy magnetic field of 0.4 μG was reported (Giovannini et al. 1993). These calculations typically assume $k = 1$, $\phi = 1$, $\nu_{\rm low} = 10$ MHz, $\nu_{\rm high} = 10$ GHz, where k is the ratio of energy densities in relativistic protons to those in electrons, ϕ is the volume filling factor, $\nu_{\rm low}$ is the low-frequency cut-off for the integral, and $\nu_{\rm high}$ is the high-frequency cut-off.

All of these parameters are poorly constrained, however the magnetic field strength behaves as these parameters raised to 2/7 power. For example, using a value of $k \sim 50$, as observed for galactic cosmic rays, increases the field by a factor of three. There is a method for estimating magnetic fields in the Coma cluster radio halo independent of minimum-energy assumptions. The analysis are based on considerations of the observed radio and X-ray spectra, the electron inverse Compton and synchrotron radiative lifetimes, and reasonable mechanisms for particle reacceleration. It was concluded (Brunetti 2001) that the fields vary smoothly from 2 $\pm$1 μG in the cluster center, to 0.3$\pm$ 0.1 μG at 1 Mpc radius. The available data suggests that radio halos seem to be strictly related to the X-ray properties of the host clusters and to the presence of cluster merger processes, which can provide energy for the electron re-acceleration and magnetic field amplification on large scales. On energetic grounds, mergers can indeed supply enough kinetic energy for the maintenance of a radio halo, as first suggested by previous studies (Harris, Kapahi, and Ekers 1980). The observed link between radio halos and cluster mergers is in favor of primary electron models. These are also supported by the high frequency steepening of the integrated radio spectra, e.g., in Coma C37, and by the radial steepening of the two frequency spectra in Coma C34, A66575 and A216375. These spectral behaviors can be easily reproduced by models that invoke the re-acceleration of particles. In contrast, they are difficult to explain by models considering secondary electron populations. Although they are not a common phenomenon in GCs, the presence of halos is a direct evidence of the presence of a magnetic field in the CG as they are location were synchrotron emission is present and thus a magnetic field.

2.2.2 Radio Mini-Halos

There are a few clusters where the relativistic electrons can be traced out quite far from the central galaxy, forming what is called mini-halo. Mini-halos are diffuse steep-spectrum radio sources, extended on a moderate scale up to $\simeq$ 500 kpc, surrounding a dominant radio galaxy at the cluster center.

Unlike radio halos, mini-halos are not tied to on-going merger events in clusters, as they are typically found at the center of the cooling core, i.e, relaxed, clusters. The prototype example of a mini-halo is at the center of the Perseus cluster (Govoni 2018). The size is $\sim$ 450 kpc, with no significant polarization. The strong polarized emission, detected through the entire cluster at 92 cm, at a Faraday depth $\sim$ 25-90 rad m^{-2} higher than the galactic contribution seems not to be related to the mini-halo. Other examples of mini-halos are in Virgo, and possibly A239043. The mini-halo in A2390 is polarized at levels of 10-20%. Previous studies suggested that the electrons of the Perseus mini-halo cannot be supplied by the central radio galaxy, but are continuously undergoing re-acceleration due to the magnetohydrodynamic (MHD) turbulence associated with the cooling flow region. They show that an isotropic magnetic field compression appears to reproduce the observed surface brightness profile and total synchrotron spectrum along with the radial spectral steepening (Govoni 2018).

On the other hand, the radial compression of the magnetic field does not appear to be applicable to the mini-halo in the Perseus cluster. The above model was successfully applied also to the mini-halo in A2626. However, the possibility that relativistic electrons in mini-halos are of secondary origin and thus produced from the interaction of cosmic ray protons with the ambient thermal protons was discussed. (Carilli and Taylor 2002; Govoni 2018).

2.2.3 Radio Relics

Possibly related phenomena to radio halos is a class of sources found in the outskirts of clusters known as **radio relics**. Like the radio halos, these are very extended sources without an identifiable host galaxy. Unlike radio halos, radio relics are often elongated or irregular in shape and they are located at the cluster periphery also their emission is strongly polarized. As the name implies, one of the first explanations put forth to explain these objects was that these are the remnants of a radio jet associated with an AGN that has since turned off. A problem with this model is that, once the energy source is removed, the radio source is expected to fade on a timescale $\sim 10^8$ yrs due to adiabatic expansion, inverse Compton, and synchrotron losses. This short timescale precludes significant motion of the host galaxy from the vicinity of the radio source. A more compelling explanation is that the relics are the result of first order Fermi acceleration of relativistic particles in shocks produced during cluster mergers, or are fossil radio sources revived by compression associated with cluster mergers. Equipartition field strengths (for more see sec. 2.4) for relics range from 0.4-3.0 μG. If the relics are produced by shock or compression during a cluster merger,then calculate a pre-shock cluster magnetic field strength in the range 0.2-0.5 μG (Carilli and Taylor 2002; Govoni 2018).

2.3 Homogenous and isotropic populations with a power-law energy distribution

For an homogeneous and isotropic population of electrons with a power-law energy distribution, i.e., with the particle density between E and $E + dE$ given by

$$n(E)dE = {N_0}^{-\delta} dE \tag{2.7}$$

the intensity spectrum, in regions which are optically thin to their own radiation, varies as follows:

$$S(\nu) \propto \nu^{-\alpha} \tag{2.8}$$

where the spectral index is $\alpha = (\delta - 1)/2$. Below the frequency where the synchrotron emitting region becomes optically thick, the total intensity spectrum can be described by:

$$S(\nu) \propto \nu^{+5/2}. \tag{2.9}$$

The synchrotron emission radiating from a population of relativistic electrons in a uniform magnetic field is linearly polarized (Govoni 2018).
In the optically thin case, the degree of intrinsic linear polarization for a homogeneous and isotropic distribution of relativistic electrons with a power-law spectrum as in the equation above is:

$$P_{\rm Int} = \frac{3\delta + 3}{3\delta + 7} \tag{2.10}$$

with the electric polarization vector perpendicular to the projection of the magnetic field onto the plane of the sky. For typical values of the particle spectral index, the intrinsic polarization degree is $\sim$ 75-80%.
In the optically thick case:

$$P_{\rm Int} = \frac{3}{6\delta + 13} \tag{2.11}$$

and the electric vector is parallel to the projected magnetic field.

In practice, the polarization degree detected in radio sources is much lower than expected by the above equations. The reduction in polarization could be due to a complex magnetic field structure whose orientation varies either with depth from the source or over the angular size of the beam. For instance, if one describes the magnetic field inside an optically thin source as the superposition of two components, one uniform, labeled as B_u; the other isotropic and random, labeled as B_r, the observed degree of polarization can be approximated by

$$P_{\rm Obs} = \frac{P_{\rm Int} {B_{\rm u}}^2}{{B_{\rm u}}^2 + {B_{\rm r}}^2}. \tag{2.12}$$

A rigorous treatment of how the degree of polarization is affected by the magnetic field configuration is presented in the following figure.

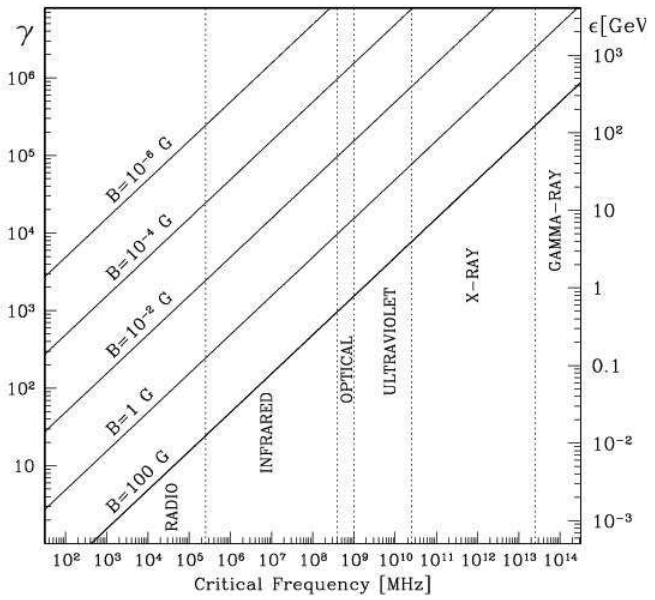

Figure 2.2: Electron Lorentz factor $\gamma = \varepsilon / m_e c^2$ (left-hand axis) and energy (right-hand axis) versus synchrotron critical frequency for magnetic field strengths in the range $10^{-6} - 10^2$ G($\theta = 90^\circ$) (Carilli 2002).

2.4 Equipartition magnetic fields derived from the synchrotron emission

From the synchrotron emissivity, it is not possible to derive unambiguously the magnetic field value. The usual way to estimate the magnetic field strength in a radio source is to minimize its total energy content $U_{\rm tot}$. The total energy of a synchrotron source is the sum of the energy in relativistic particles $U_{\rm el}$, in electrons, and $U_{\rm pr}$, in protons, and the energy in its magnetic fields $U_{\rm B}$, see fig. 2.3:

$$U_{\rm tot} = U_{\rm el} + U_{\rm pr} + U_{\rm B}. \tag{2.13}$$

The magnetic field energy contained in the source of volume V is given by:

$$U_{\rm B} = \frac{B^2}{8\pi}\phi V \tag{2.14}$$

where ϕ is the fraction of the source volume occupied by the magnetic field (filling factor).
The total electron energy in the range E_1-E_2:

$$U_{\rm el} = V\int_{E_2}^{E_1} N(E)EdE = VN_0\int_{E_2}^{E_1} E^{-\delta+1}dE \tag{2.15}$$

can be expressed as a function of the synchrotron luminosity $L_{\rm syn}$:

$$L_{\rm syn} = V \times \int_{E_2}^{E_1}(-\frac{dE}{dt})N(E)dE = c_2(B\sin\theta)^2 VN_0\int_{E_2}^{E_1} E^{-\delta+1}dE. \tag{2.16}$$

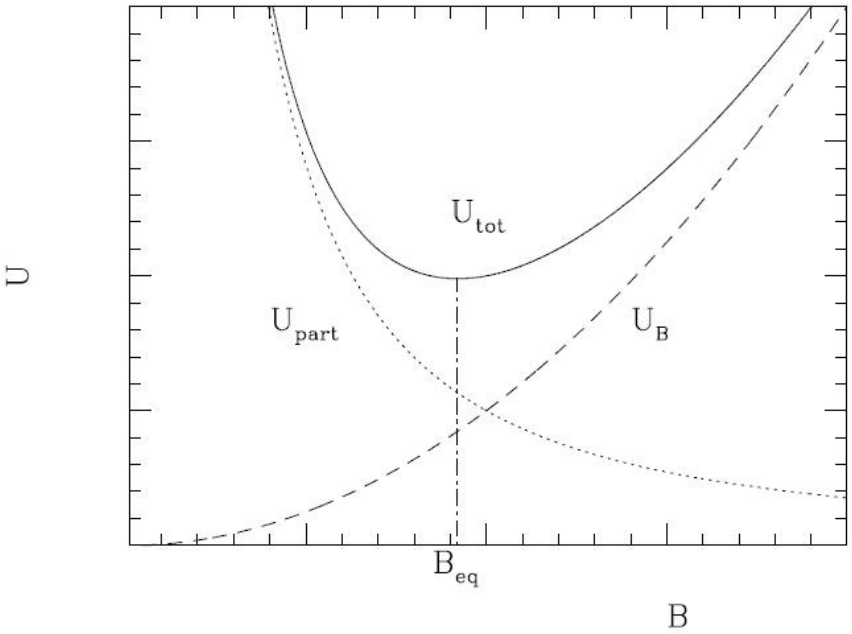

Figure 2.3: Energy content in a radio source. The energy in the magnetic fields is $U_{\rm B} \propto B^2$, the energy in the relativistic particles is $U_{\rm part} = U_{\rm el} + U_{\rm pr} \propto B^{-3/2}$. The total energy content $U_{\rm tot}$ has a minimum when the contributions of the magnetic fields and the relativistic particles are approximately equal. This magnetic field is referred to as the equipartition value $B_{\rm eq}$ (Carilli 2002).

By eliminating V, N_0 and by writing E_1 and E_2 in terms of ν_1 and ν_2 in the previous equation the following result is obtained:

$$U_{\rm el} = {c_1}^{-1}{c_2}^{-1/2} C(\alpha,\nu_1,\nu_2) L_{\rm syn} B^{-3/2} = c_{12}(\alpha,\nu_1,\nu_2) L_{\rm syn} B^{-3/2} \tag{2.17}$$

where $\sin\theta = 1$ is taken and:

$$C(\alpha,\nu_1,\nu_2) = \frac{2\alpha-1}{2\alpha-1}\frac{{\nu_1}^{(1-2\alpha)/2} - {\nu_2}^{(1-2\alpha)/2}}{{\nu_1}^{1-\alpha} - {\nu_2}^{(1-\alpha)}}. \tag{2.18}$$

The energy contained in the heavy particles, $U_{\rm pr}$, can be related to $U_{\rm el}$ assuming:

$$U_{\rm pr} = kU_{\rm el}$$

Finally, the total energy is obtained as a function of the magnetic field:

$$U_{\rm tot} = (1+k)c_{12}L_{\rm syn}B^{-3/2} + \frac{B^2}{8\pi}V\phi \tag{2.19}$$

To obtain an estimation of the magnetic field, it is necessary to make some assumptions about how the energy is distributed between the field and particles. A convenient estimation for the total energy is represented by its minimum value(Govoni 2018). The condition of minimum energy is obtained when the contributions of the magnetic field and the relativistic particles are approximately equal:

$$U_{\rm B} = \frac{3}{4}(1+k)U_{\rm el}. \tag{2.20}$$

For this reason, the minimum energy is also known as the equipartition value:

$$U_{\rm tot}(min) = \frac{3}{4}(1+k)U_{\rm el} = \frac{7}{3}U_{\rm B}. \tag{2.21}$$

The magnetic field for which the total energy content is minimum is:

$$U_{\rm eq} = (6\pi(1+k)c_{12}L_{\rm syn}\phi^{-1}V^{-1})^{2/7}. \tag{2.22}$$

The total minimum energy is:

$$U_{\rm tot}(min) = c_{13}(\frac{3}{4\pi})^{3/7}(1+k)^{4/7}\phi^{3/7}V^{3/7}{L_{\rm syn}}^{4/7} \tag{2.23}$$

and the total minimum energy density is:

$$u_{\rm min} = \frac{U_{\rm tot}(min)}{V\phi} = c_{13}(\frac{3}{4\pi})^{3/7}(1+k)^{4/7}\phi^{-4/7}V^{-4/7}{L_{\rm syn}}^{4/7} \tag{2.24}$$

where $c_{13} = 0.921{c_{12}}^{4/7}$. The constants c_{12} and c_{13}, depend on the spectral index and the frequency range. Including the K-correction, assuming $\phi = 1$, and expressing the various parameters in commonly used units, the minimum energy density of a radio source in terms of observed quantities can be written:

$$u_{\rm min} = \xi(\alpha,\nu_1,\nu_2)(1+k)^{4/7}{\nu_0}^{4\alpha/7}(1+z)^{(12+4\alpha)/7} \times {I_0}^{4/7}d^{-4/7} \tag{2.25}$$

where z is the source redshift, I_0 is the source brightness at the frequency ν_0, d is the source depth, and the constant $\xi(\alpha, \nu_1, \nu_2)$ is tabulated, fig. 2.4 for the frequency ranges: 10 MHz - 10 GHz and 10 MHz - 100 GHz. I_0 can be

measured directly from the contour levels of radio images for significantly extended sources, or it can be obtained by dividing the total flux of the source by the solid angle of the source. The equipartition magnetic field is then obtained as:

$$B_{\rm eq} = \left(\frac{24\pi}{7} u_{\rm min}\right)^{\frac{1}{2}}. \tag{2.26}$$

Various uncertainties come from this determination of the magnetic field strength. The value of k and the ratio of the energy of relativistic protons to electrons depends on the mechanism of generation of relativistic electrons and while some possibilities have been put forward (sec. 1.1) further studies need to be done, which is so far poorly known. Other uncertainties are also related to the filling factor ϕ. The values assumed typically in the literature for CGs are $k = 1$ (or $k = 0$) and $\phi = 1$. Another difficult parameter to establish is the extent of the source along the line of sight d.

α	$\xi(\alpha$, 10 MHz, 10 GHz)	$\xi(\alpha$, 10 MHz, 100 GHz)
0.0	1.43×10^{-11}	2.79×10^{-11}
0.1	9.40×10^{-12}	1.63×10^{-11}
0.2	6.29×10^{-12}	9.72×10^{-12}
0.3	4.29×10^{-12}	5.97×10^{-12}
0.4	2.99×10^{-12}	3.79×10^{-12}
0.5*	2.13×10^{-12}	2.50×10^{-12}
0.6	1.55×10^{-12}	1.72×10^{-12}
0.7	1.15×10^{-12}	1.23×10^{-12}
0.8	8.75×10^{-13}	9.10×10^{-13}
0.9	6.77×10^{-13}	6.92×10^{-13}
1.0*	5.32×10^{-13}	5.39×10^{-13}
1.1	4.24×10^{-13}	4.27×10^{-13}
1.2	3.42×10^{-13}	3.43×10^{-13}
1.3	2.79×10^{-13}	2.79×10^{-13}
1.4	2.29×10^{-13}	2.29×10^{-13}
1.5	1.89×10^{-13}	1.89×10^{-13}
1.6	1.57×10^{-13}	1.57×10^{-13}
1.7	1.31×10^{-13}	1.31×10^{-13}
1.8	1.10×10^{-13}	1.10×10^{-13}
1.9	9.21×10^{-14}	9.21×10^{-14}
2.0	7.76×10^{-14}	7.76×10^{-14}

Figure 2.4: Equipartition parametrization for these values of α the constant defined in eq. 2.18 diverges; thus the corresponding parameters have been computed by solving directly the integrals in eq. 2.15 and 2.16 (Govoni 2018).

In the approach presented above, the computation of the equipartition parameters is based on the integration of the synchrotron radio luminosity between the two fixed frequencies ν_1 and ν_2. The electron energies that correspond to these frequencies depend on the magnetic field value, and thus the integration limits are variable in terms of the energy of the radiating electrons. The lower limit is particularly relevant, because of the power-law shape of the electron energy distribution and the fact that electrons of very low energy are expected to be present. If a low-energy cutoff in the particle energy distribution is imposed, rather than a low-frequency cutoff in the emitted synchrotron spectrum, the exponent $\frac{2}{7}$ should be replaced by $\frac{1}{(3+\alpha)}$, as pointed out by previous studies (Carilli and Taylor 2002). The equipartition quantities obtained following this approach are presented (Brunetti 2001). Indicating the electron energy by its Lorentz factor γ and assuming that $\gamma_{\rm min} \ll \gamma_{\rm max}$, the new expression for the

equipartition magnetic field B^1_{eq} in Gauss is (for $\alpha > 0.5$):

$$B^1{}_{\rm eq} \sim \gamma_{\rm min}{}^{\frac{1-2\alpha}{3+\alpha}} B_{\rm eq}{}^{\frac{7}{2(2+\alpha)}} \tag{2.27}$$

where $B_{\rm eq}$ is the value of the equipartition magnetic field. If this value for the field, obtained with the standard formulas, is of the order of μG the magnetic field derived considering $\gamma_{\rm min} \sim 100$ is 2-5 times larger using $\alpha \in [0.75, 1]$.

2.5 Inverse Compton radiation

Through the IC effect, relativistic electrons in a radiation field can scatter and transfer energy to photons. This is an important mechanism for the electron population responsible for the scattering of synchrotron emission from microwave background photons (T = 2.73 K). At the frequency of ($\nu \sim 10^{11}$Hz) the relativistic electrons are related to $\gamma \sim$ 1000-5000 and are responsible for IC emission in the X-ray domain. Assuming a power law for the electron energy, the spectral index α is related to the power law index as $\delta = 2\alpha + 1$ and the photon index of the IC motion as $\Gamma_X = \alpha + 1$.

The IC emissivity is proportional to the energy density of the photon field u_{ph}, while the synchrotron emissivity is proportional to the energy density (an assumption of equipartition of energy was made) in the magnetic field $u_B \propto \frac{B^2}{8\pi}$ (Govoni 2018).

$$\frac{L_{syn}}{L_{IC}} \propto \frac{u_B}{u_{ph}}. \tag{2.28}$$

The syncrotron flux at the frequency in radio ν_r and at the frequency in X ν_X are:

$$S_{syn}(\nu_r) = 1.7 \times 10^{-21} \frac{VN_0}{4\pi D^2} a(\delta) B^{1+\alpha} \left(\frac{4.3 \times 10^6}{\nu_r}\right)^{\alpha} \tag{2.29}$$

$$S_{IC}(\nu_X) = 4.2 \times 10^{-40} \frac{VN_0}{4\pi D^2} b(\delta) B^{1+\alpha} T^{3+\alpha} (1+z)^{3+\alpha} \left(\frac{2.1 \times 10^{10}}{\nu_X}\right)^{\alpha} \tag{2.30}$$

where $a(\delta)$ and $b(\delta)$ are functions α, δ-dependent; V is the emission volume; D is the source distance. From the ratio it is possible to evaluate the magnetic field:

$$B^2 = 10^{-16} \frac{S_{syn}(\nu_r)}{S_{IC}(E_1 - E_2)} (1+z)^4 \nu_r ln \frac{E_2}{E_1} \tag{2.31}$$

where the flux S_{IC} is integrated between a energy interval $E_1 - E_2$ (in keV), $\alpha = 1$. The result of B is in μG. This method presents some flaws, the first one being the current technological limitations for hard X-ray domain observations, and the second one being the problem of distinguishing thermal and non-thermal sources X-ray emission. In the particular case of detecting from a non-radio emitting region, only a lower limit of the magnetic field can be derived (Govoni 2018).

2.6 Faraday Rotation Effect

Faraday rotation effect appears during the propagation of electromagnetic waves in a magnetized plasma, right-handed and left-handed circularly polarized waves propagate with different phase velocities within the magnetic charged material. The plane of polarization of the electromagnetic wave is rotated due to this effect (Govoni 2018).

$$n_{L,R} = \left(1 - \frac{\nu_p^2}{\nu^2 \pm \omega \nu_g}\right)^{1/2} \tag{2.32}$$

where $\omega = 2\pi\nu$ is the angular frequency of the wave; $\omega_p = \sqrt{\frac{4\pi n_e e^2}{m_e}}$ is the plasma frequency; and $\nu_g = \frac{eB}{m_e c}$ is the cyclotron frequency.

To study cluster magnetic fields, we are interested in the Faraday rotation of radio sources in the background of the

cluster or in the cluster itself. For the typical value in the ICM, $B \simeq 1$ μG, $n_e \simeq 10^{-3}$ cm^{-3}, the limit $\nu \gg \nu_g$ can be used and the previous equation becomes:

$$n_{L,R} \approx 1 - \frac{1}{2}\frac{\nu_p^2}{\nu^2 \pm \omega\nu_g} \tag{2.33}$$

and the difference of time of the two opposite handed waves to travel a path length, dl, with a phase difference of $\Delta\phi = \nu\Delta t$, is:

$$\Delta t \approx \frac{\nu_p^2 \nu_g dl}{c\omega^3} = \frac{4\pi e^3}{\nu^3 m_e^2 c^2} n_e B dl. \tag{2.34}$$

Then :

$$\chi_{obs}(\lambda) = \chi_0 + \Delta\chi = \chi_0 + \lambda^2 RM, \tag{2.35}$$

where χ_0 is the intrinsic polarization angle, RM is the rotation measure (rad m^{-2}):

$$RM = \frac{e^3}{2\pi m_e^2 c^4} \int_0^L n_e(l) B_{||}(l) dl. \tag{2.36}$$

More simply:

$$RM = 812 \int n_e B_{||} dl. \tag{2.37}$$

The Faraday rotation can induce a depolarization of the observed radiation in different circumstances. The depolarization can be due to limitations of instrumental capabilities or/and due to the presence of fluctuations, and due to internal factors. The results in a reduction of the observed degree of polarization. In the case that the Faraday effect originates entirely within the source, when the source can be represented by a homogeneous optically thin slab, the degree of polarization varies as

$$P_{obs}(\lambda) = P_{int} \frac{\sin(RM'\lambda^2)}{RM'\lambda^2} \tag{2.38}$$

where RM' is the internal rotation measure through the depolarization source, $RM' = 2RM_{obs}$.

2.6.1 Interpretation of the cluster RM data

RM data of radio sources in the background of clusters or in the clusters themselves can provide important information on the cluster magnetic field responsible for the Faraday effect. The Faraday effect of a uniform magnetic field does not produce a depolarization, neither a rotation of the polarization angle proportional to $\lambda\langle RM\rangle$:

$$\langle RM\rangle = 812 B_{||} n_e L. \tag{2.39}$$

In the simplest approximation, the magnetic field is tangled on a single scale Λ_c. The distribution of the RM is Gaussian with $\langle RM\rangle$=0 the variance is:

$$\sigma_{RM}^2 = 812^2 \Lambda_c \int (n_e B_{||})^2 dl. \tag{2.40}$$

By considering a density distribution with a β-profile:

$$n_e(r) = n_0 (1 + \frac{r^2}{r_c^2})^{\frac{-3\beta}{2}} \tag{2.41}$$

and by integrating 2.40

$$\sigma_{RM}(r_\perp) = \frac{KBn_0 r_c^{1/2}\Lambda_c^{1/2}}{(1+\frac{r_\perp^2}{r_c^2})^{\frac{6\beta-1}{4}}}\sqrt{\frac{\Gamma(3\beta-\frac{1}{2})}{\Gamma(3\beta)}} \tag{2.42}$$

where Γ is the Gamma function, K depends on the integration path over the gas varying from 624 if the source is beyond the cluster and 441 is the source is halfway through the cluster (Govoni 2018).

2.7 Faraday Rotation Measure Synthesis

As described above, Faraday rotation occurs due to the birefringence of the magneto-ionic medium, the polarization angle of linearly polarized radiation that propagates through the plasma is rotated as a function of frequency. Assuming that the directions of the velocity vectors of the electrons gyrating in a magnetized plasma are isotropically distributed, eq. 2.10 shows that the intrinsic degree of polarization of the synchrotron radiation from the plasma in a uniform magnetic field is given by independent of frequency and viewing angle. Integrating eq. 2.7 so that it gives the total electron density:

$$n_e = \int_{E_0}^{+\infty} n_e(E)dE \tag{2.43}$$

where E_0 is a cutoff energy that is required in order to let the integral converge. From observations of the Crab nebula it was determined that $\delta \simeq \frac{5}{3}$ (Westfold 1959). This would imply a polarization fraction of approximately 67%, independent of frequency. In many radio sources, the observed polarization fractions are much lower. Usually the polarization fraction decreases steeply with increasing wavelength. This depolarization effect taken into discussion is the Faraday dispersion, i.e, emission at different Faraday depths along the same line of sight (Burn 1966). We make a clear distinction between Faraday depth (ϕ) and RM, already discussed in sec. 2.6 and 2.6.1. The Faraday depth of a source can be defined as:

$$\phi = 0.81 \int n_e B dl \quad \text{rad}\cdot\text{m}^{-2} \tag{2.44}$$

where n_e is the electron density in cm^{-3}, B is the magnetic induction in μG and dl is an infinitesimal path length in parsecs. A positive Faraday depth implies a magnetic field pointing towards the observer. There may exist many different sources of radiation at different Faraday depths along the same line of sight. These sources may be either Faraday thin or Faraday thick. A source is Faraday thin if:

$$\lambda^2 \Delta\phi \ll 1. \tag{2.45}$$

$\Delta\phi$ denotes the extent of the source in ϕ, and λ is the wavelenght. Faraday thin sources are well approximated by Dirac δ-functions of ϕ. A source is Faraday thick if

$$\lambda^2 \Delta\phi \gg 1. \tag{2.46}$$

Faraday thick sources are extended in ϕ. They are substantially depolarized at λ^2. Remember that whether a source is Faraday thick or Faraday thin is wavelength dependent. A different way to express eq. 2.36 can be:

$$RM = \frac{d\chi(\lambda^2)}{d\lambda^2} \tag{2.47}$$

where χ is the slope of the polarization angle and, of course λ is the wavelenght. χ is given by:

$$\chi = \frac{1}{2}\tan^{-1}\frac{U}{Q}. \tag{2.48}$$

If the line of sight has only one source, which in addition has no internal Faraday rotation, and does not suffer from beam depolarization, then the Faraday depth of that source is equal to its rotation measure at all wavelengths (Brentjens and Bruyn 2005):

$$\chi(\lambda^2) = \chi_0 + \phi\lambda^2. \tag{2.49}$$

Now, by combining equation eq. 2.47 and 2.49 :

$$RM = \phi. \tag{2.50}$$

2.8 Cold fronts

In Clusters, such as A2142 and A3667, a sharp discontinuity in the X-ray surface brightness was observed (Markevitch et al. 2000), the so called *cold fronts*. The observed temperature jumps and it is required that the thermal conduction must be suppressed by two orders of magnitude relative to the classical Spitzer value. If not, cooler structures on scales of ~ 0.1 Mpc will be evaporated by thermal conduction from the hot surrounding medium on timescales of $\sim 10^7$ yrs. A tangled magnetic field has been shown to reduce the thermal conductivity from the Spitzer value by a factor of 10^2-10^3 (Chandran and Cowley 1998).
These structures are contact discontinuities between the gas which was in the cool core of one of the merging sub-clusters and the surrounding intracluster gas. They are not shocks because the density increase across the front is accompanied by a temperature decrease such that there is no dramatic change in the pressure and entropy. It was found that the front sharpness and its gradual smearing at large angles are most likely explained by the existence of a layer with a ~ 10 μG magnetic field parallel to the front. These structures are interpreted as resulting from cluster mergers, where a cooler subcluster core falls into a hot ICM at sub-sonic or trans-sonic velocities ($\sim 10^3$ km s^{-1}). A discontinuity is formed where the internal pressure of the core equals the combined ram and thermal pressure of the external medium. Gas beyond this radius is stripped from the merging subcluster, and the core is not penetrated by shocks owing to its high internal pressure. The best example of a cluster cold front is that seen in Abell 3667 (fig. 2.5) (Vikhlinin 2001). In this case, the temperature discontinuity occurs over a scale of 0.5 kpc, comparable to the collisional mean free path of just a few kpc for a typical cluster, thereby it requires thermal isolation. Magnetic fields play a fundamental role in allowing for such structures in two ways (Vikhlinin 2001):

- by suppressing thermal conduction,
- by suppressing Kelvin-Helmholtz mixing along the contact discontinuity.

A model is also presented, in which the field is tangentially sheared by fluid motions along the contact discontinuity. They invoke magnetic tension to suppress mixing, and show that the required magnetic pressure is between 10% and 20% of the thermal pressure. The implied fields are between 7 and 16 μG. They also argue that the fields cannot be much stronger than this, because dynamically dominant fields would suppress mixing along the entire

front, which does not appear to be the case. The existence of cold fronts provides strong evidence for cluster magnetic fields. However, the field strengths derived correspond to those in the tangentially sheared boundary region around the front. Relating these back to the unperturbed cluster field probably requires a factor of a few reduction in field strength, implying unperturbed field strengths between 1 and 10 μG, although the exact scale factor remains uncertain.

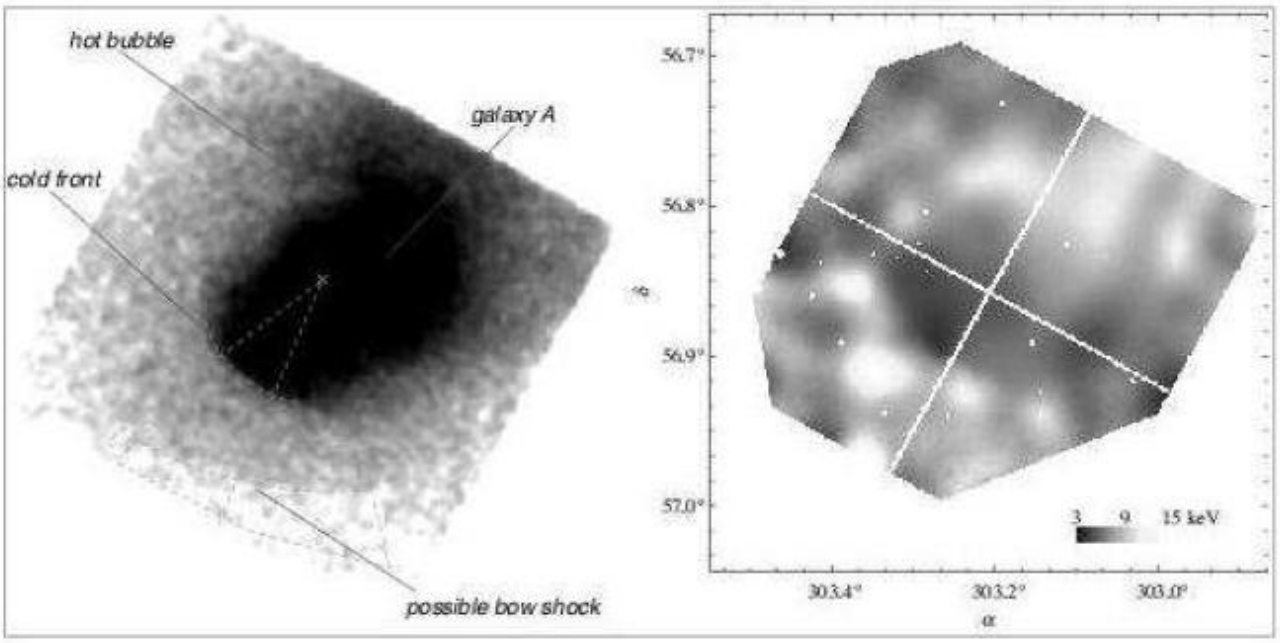

Figure 2.5: Chandra X-ray image (left) and temperature map (right) of the cluster A3667 (Vikhlinin 2001).

2.9 Magnetic field profile

The simplest model for a cluster magnetic field is a uniform field through the whole cluster, that is not realistic. Faraday rotation measurements of radio sources in rich clusters indicate that the general cluster magnetic field is probably highly tangled (Jaffe 1980).

The magnetic field distribution in a cluster depends on the thermal gas density and on the distribution of massive galaxies and therefore declines with the cluster radius. A radial decrease of the cluster magnetic field strength is also deduced in the framework of halo formation models which consider the reacceleration of the radio emitting electrons. Indeed, the spatial correlation found in some clusters between the X-ray cluster brightness and the radio halo brightness implies that the energy densities in the thermal and non-thermal components have a similar radial scaling, thus a magnetic field decline is inferred. A radial decrease of the cluster magnetic field strength is also deduced in the framework of halo formation models which consider the reacceleration of the radio emitting electrons. The radial steepening of the synchrotron spectrum, observed in the Coma cluster and more recently in A665 and A2163, is interpreted as the result of the combination of the magnetic field profile with the spatial distribution of the reacceleration efficiency, thus allowing us to set constraints on the radial profile of the cluster magnetic field. In fig. 2.6 the magnetic field profile in the by applying a model for the electron reacceleration is shown (Brunetti 2001). Different lines refer to different values of the reacceleration coefficient. The field intensity is found to decrease smoothly from $\sim$ 0.5-1.5 μG at the cluster center to $\sim$ 0.03-0.5 μG at $\sim$ 1.3 Mpc radius, with a trend similar to that of the thermal gas.

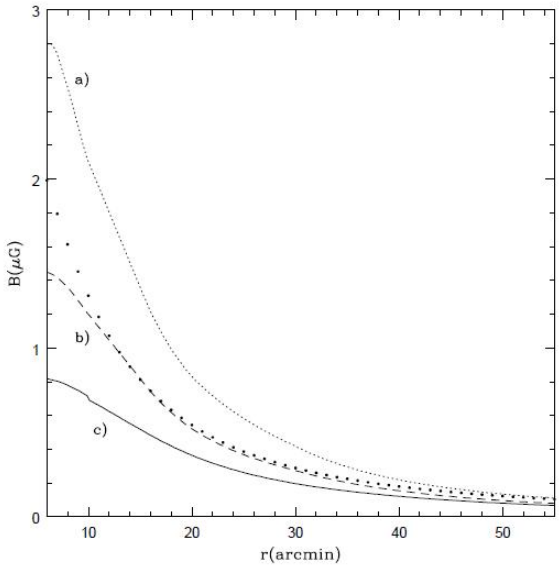

Figure 2.6: The magnetic field profile in the Coma cluster obtained from the radial spectral steepening, by applying an electron reacceleration model. H_0 = 50 km s^{-1} Mpc^{-1} is being used. The trends, however, do not depend on the assumed cosmology. Different lines refer to different values of the reacceleration coefficient (Vikhlinin 2001; Brunetti 2001).

3. Theoretical Background Related to Axion-like Particles

3.1 What are Axion-like Particles?

The **Axion** is a fundamental particle introduced to solve the unexplained missing CP-symmetry violation in strong interactions. This violation is not forbidden by the Standard Model (SM) of particle physics. A violation of the *Parity*× *Charge* symmetry (CP) is not experimentally seen in *Quantum Chromo-Dynamics* (QCD). The term of the Lagrangian corresponding to the CP violation can be written as:

$$\mathscr{L}_{\theta_{QCD}} = \theta_{QCD}\frac{g^2}{32\pi^2}G^a_{\mu\nu}\tilde{G}^{\mu\nu}_a \tag{3.1}$$

where θ_{QCD} is a phase parameter of QCD, G is the gluon field strength tensor, the index a is related to the trace summation over the SU(3) colors and g^2 is the QCD coupling constant. If θ_{QCD} is zero, no CP violation is present. Peccei and Quinn (PQ) proposed a mechanism to solve this Strong CP Problem by the introduction of a new global symmetry, known as U(1)$_{PQ}$ symmetry, in order to make the CP-violating term in the QCD Lagrangian negligible, eq. 3.1. By following the PQ mechanism, axions are *pseudo-Nambu-Goldstone bosons* associated with the breaking of the U(1)$_{PQ}$ symmetry.

In the PQ formalism, the axion has a mass $m_a \sim 100$ keV and a decay constant f_a, related to the decay amplitude, to the coupling. In the original model of the axion proposed (Peccei and Quinn 1977) the axion decay constant f_a is of the order of the electroweak (ELW) scale (∼246 GeV), and the mass of the axion m$_a$ is inversely proportional to this, $m_a \sim 100$ keV.

$$m_a \simeq 6\times10^{-6}\text{eV}(\frac{10^{12}GeV}{f_a}) \tag{3.2}$$

By basing the estimation on the experimental limits related to the stellar evolution and rare particle decays, the PQ model was ruled out. New models were presented, the Kim-Shifman-Vainshtein-Zakharov model (KSVZ) (Kim 1979) and the Dine-Fischler-Srednicki-Zhitnitsky model (DFSZ) (Dine, Fischler, and Srednicki 1981). In both models, the energy scale of the symmetry breaking was proposed to be large, close to the *Grand Unification scale* (GUT), at the energy of 10^{15} GeV. This modifies the axion mass scale that becomes a very light axion, $m_a \simeq 10^{-9}$eV. These axions would have a very weakly coupling, therefore, it is named *invisible axion*. Due to their values of mass and coupling, these axions would be eluded in several experiments. After several unsuccessful searches for axions (see fig. 3.1 for a collection of limits), the axion model was extended to a wider group of particles, called **Axion-Like Particles** (ALPs), in which the decay constant is no longer coupled with the mass, differently from the original axion (Eq. 3.2) (Arias et al. 2012; Batković et al. 2021).

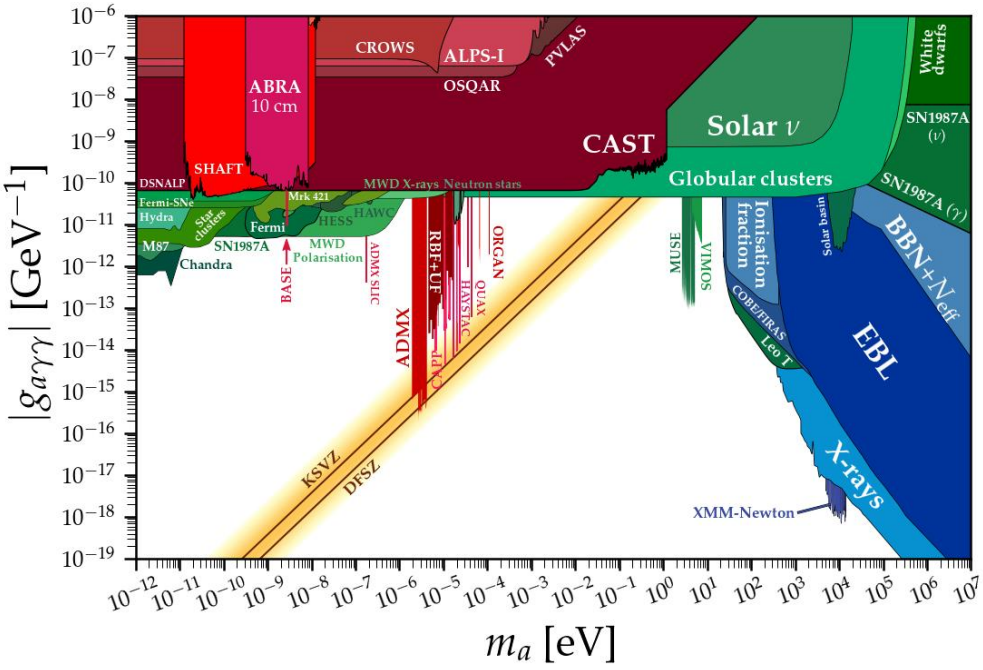

Figure 3.1: ALPs parameter space with current constraints (updated August 2022). The collected limits, references, and plots are available on https://cajohare.github.io/AxionLimits/.

The term on the y-axis in fig. 3.1 $g_{a_{\gamma\gamma}}$ is the axion-photon coupling, also seen through the two-photon vertex in fig. 3.2. This term is used in:

$$\mathscr{L}_{a_{\gamma\gamma}} = -\frac{g_{a_{\gamma\gamma}}}{4} F_{\mu\nu}\tilde{F}^{\mu\nu} = g_{a_{\gamma\gamma}}\vec{E}\cdot\vec{B}a \tag{3.3}$$

Other than the ALP-Phton coupling, in the equation are present:

- $F_{\mu\nu}$ is the strength tensor of the electromagnetic field;
- $\tilde{F}_{\mu\nu}$ is the dual of the strength tensor;
- a is the axion field its respective mass m_a;
- $\vec{E}$ is the electric field of a beam photon;
- $\vec{B}$ is the external magnetic field.

This effect, explained as the photon-ALP conversion, occurs in magnetic fields and is the basis of many experiments in the search for ALPs.

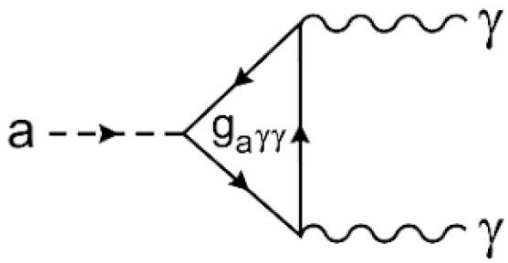

Figure 3.2: Feynman diagram of the photon-axion coupling vertex.

Today, axions are also proposed as possible DM particle candidates. The reason is related to the their small mass, combined with a possibly large decay constant $f_a \simeq 10^{12}$ GeV. Since they are connected to spontaneous symmetry breaking, they could have been produced in the early Universe via *misalignment mechanisms*. They could represent a substantial fraction of DM, it is reported that (Arias et al. 2012), in order to explain the current amount of DM with ALPs, the axion coupling, dependent on the mass of axions, has to be:

$$g_{a_{\gamma\gamma}} < 10^{-12}[\frac{m_a}{1\text{neV}}]^{\frac{1}{2}}\text{GeV}^{-1} \tag{3.4}$$

Together with hidden photons, axions could be used as viable candidates for DM, and they are named **Very Weakly Interacting Slim Particles** (WISPs). Searches for axion and ALPs are based on the analysis of cosmic magnetic fields and ample photon fluxes present in the cosmos. Clusters of galaxies have been chosen in this research as they are good subjects, having strong magnetic fields at their cores that are orders of magnitude larger than the average ICM (Marsh et al. 2017). Alternative subjects are magnetic fields in active galactic nuclei or pulsars could also be considered as a possible *medium* for the conversion of photons to axions or ALPs (Batković et al. 2021).

3.2 Mixing between γ-rays and ALP in an Astrophysical Environment

The existence of axions and ALPs can be probed by their imprints on the spectra of astrophysical sources. ALPs couple with photons in the presence of magnetic fields. Therefore, TeV γ-rays travelling over cosmological distances can oscillate to photons due to the interaction with magnetic fields, and/or convert to ALPs in strong magnetic fields and cross astrophysical distances until they could encounter another strong magnetic field, such as that of the Milky Way, in which they can convert back into observable γ-rays (Batković et al. 2021). The term that governs these conversion/reconversion processes is the probability term for the mixing $P_{\gamma\gamma}$, which depends on:

- The ALP mass.
- The ALP coupling.
- The characteristics of the magnetic field.

3.2.1 ALP Propagation

To understand the phenomenon of conversion, it is necessary to compute the term $P_{\gamma\gamma}$. The photon-ALP system can be expressed with a Lagrangian:

$$\mathscr{L} = \frac{g_{a\gamma\gamma}}{4} F_{\mu\nu}\tilde{F}^{\mu\nu} a - \frac{1}{4} F_{\mu\nu}F^{\mu\nu} + \frac{\alpha^2}{90 m_e^4}\left[(F_{\mu\nu}F^{\mu\nu})^2 + \frac{7}{4}(F_{\mu\nu}\tilde{F}^{\mu\nu})^2\right] + \frac{1}{2}(\partial_\mu a \partial^\mu a - m_a^2 a^2) \tag{3.5}$$

where the first term was already seen in eq. 3.4 and it refers to the photon–ALP coupling, followed by the term that relates to the effective Euler–Heisenberg Lagrangian $\mathscr{L}_{EH}$ for corrections of QED loops in photon propagators due to an external magnetic field (Raffelt and Stodolsky 1988), and the last term $\mathscr{L}_a$ describes the kinetic and mass term of the axionic field. To model the propagation, the motion of the ALP in the x_3 direction in a cold and ionized plasma was considered. The equation of motion for polarized photons and relativistic ALPs can be written as:

$$\left(i\frac{d}{dx_3} + E + \mathscr{M}\right)\begin{pmatrix} A_1(x_3) \\ A_2(x_3) \\ a(x_3) \end{pmatrix} = 0 \tag{3.6}$$

where:

- $\mathscr{M}$ is the photon-ALP mixing matrix.
- $A_1(x_3)$ and $A_2(x_3)$ are the photon linear polarization amplitudes along the x_1 and x_3 axis.
- $a(x_3)$ is the axion field strength (Meyer, Horns, and Raue 2013).

The solution to this equation is the transfer function $\mathscr{T}(x_3,\ 0;\ \mathrm{E})$ given the condition $\mathscr{T}(0,\ 0;\ \mathrm{E}) = 1$. For a homogeneous magnetic field that is transverse to the propagation direction (laying in x_2 direction) of the photon beam, the photon–ALP mixing matrix $\mathscr{M}$ can be simplified into:

$$\mathscr{M}_0 = \begin{pmatrix} \Delta_\perp & 0 & 0 \\ 0 & \Delta_\parallel & \Delta_{a_\gamma} \\ 0 & \Delta_{a_\gamma} & \Delta_a \end{pmatrix} \tag{3.7}$$

the elements in this matrix are written considering:

- The Plasma Condition.
- The QED vacuum birefringence.
- The Axion field.
- The photon-ALP mixing.

They can be written as:

$$\Delta_\perp = \Delta_{pl} + 2\Delta_{QED} \tag{3.8}$$

$$\Delta_\parallel = \Delta_{pl} + \frac{7}{2}\Delta_{QED} \tag{3.9}$$

$$\Delta_{a_\gamma} = \frac{1}{2} g_{a_{\gamma\gamma}} B_\perp \tag{3.10}$$

$$\Delta_a = -\frac{m_a^2}{2E} \tag{3.11}$$

with

$$\Delta_{pl} = -\frac{\nu_{pl}^2}{2E} \tag{3.12}$$

$$\Delta_{QED} = \frac{\alpha E B_\perp^2}{45\pi B_{CR}^2}. \tag{3.13}$$

Where:

- α is the fine structure constant.
- ν_{pl} is the plasma frequency connected to the ambient thermal electron density.
- $B_{CR} \sim 4.4 \times 10^{13}$G is the critical magnetic field term.
- Δ_{a_γ} represents the photon-ALP mixing and depends on the strength of the interaction $g_{a_{\gamma\gamma}}$ and the intensity of the transverse magnetic field $B_\perp$.

Normally, the magnetic field B does not have to be in the x_2 direction, but at an angle ψ from it. In this case, the equations of motion are solved with a transfer function $\mathscr{T}$ (x_3, 0, E; ψ) = V(ψ) $\mathscr{T}$ (x_3, 0, E) $\times$ V†(ψ) where $\mathscr{M}$ changed in $\mathscr{M}$ = V(ψ)M$_0$ V†(ψ) (Batković et al. 2021).

3.2.2 Probability of ALP-γ Conversion

By using the transfer function, the probability of the conversion of a γ-ray to an ALP in an external magnetic field can be computed. The simplest description of the magnetic field is that of a single domain. In this case, the probability of the photon–ALP mixing can be written as (Raffelt and Stodolsky 1988):

$$P_{\gamma\to a} = (\Delta_{a_\gamma} d)^2 \frac{\sin^2(\Delta_{osc}\frac{d}{2})}{(\Delta_{osc}\frac{d}{2})^2} = \sin^2(2\theta)\sin^2\Big(\frac{\Delta_{osc} d}{2}\Big) \tag{3.14}$$

where θ is the rotation angle given by the formula:

$$\theta = \frac{1}{2}\arcsin\Big(\frac{2\Delta_{a_\gamma}}{\Delta_{osc}}\Big) \tag{3.15}$$

d is the size of the domain and Δ_{osc} is the oscillation wave number :

$$\Delta^2_{osc} = [(\Delta_a - \Delta_{pl})^2 + 4\Delta^2_{a_\gamma}] \tag{3.16}$$

Δ_{osc} can be written in terms of a critical energy E_{crit} defined as:

$$E_{crit} \sim 2.5 GeV \frac{|m^2_{a,neV} - \nu^2_{pl,neV}|}{g_{11} B_{\mu G}} \tag{3.17}$$

where $\nu_{pl,neV}$ is the plasma frequency in units of neV, $B_{\mu G}$ is the magnetic field expressed in μG, the term g_{11} is expressed as:

$$g_{11} = \frac{g_{a\gamma\gamma}}{10^{-11}\text{GeV}} \tag{3.18}$$

With E_{crit}, the term Δ_{osc} can be written (Horns et al. 2012) as:

$$\Delta_{osc} = 2\Delta_{a_\gamma}\sqrt{1 + \Big(\frac{E_c}{E}\Big)^2}. \tag{3.19}$$

Around and above the E_{crit} value, the probability of conversion $P_{\gamma\to a}$ in eq. 3.14 becomes sizable.

3.2.3 γ-ray Survival Probability

The γ-ray survival probability (the fraction of photon that did not convert to ALP) can be computed. To do it, the exact morphology of the magnetic field should be taken into consideration and the hypothesis of having just one single magnetic field domain with a fixed orientation is not plausible. A common approach is to divide it into N different domains. By doing this, the transfer matrix can be reformulated (Mirizzi and Montanino 2017), thus providing the total photon survival probability $P_{\gamma\gamma}$:

$$P_{\gamma\gamma} = \frac{1}{3}\Big(1 - exp\Big(-\frac{3}{2}NP_{\gamma\to a}\Big)\Big) \tag{3.20}$$

When writing eq. 3.14 following the previously introduced substitutions, the following equation can obtained:

$$P_{\gamma\to a} = sin^2(2\theta) sin^2\Big[\frac{g_{a\gamma\gamma} Bd}{2}\sqrt{1 + \Big(\frac{E_c}{E}\Big)^2}\Big] \tag{3.21}$$

As one can see from eq. 3.21, $P_{\gamma\to a}$ depends on the product of domain length d and magnetic field B. Because of this, it is essential to have a well-defined magnetic field model to account for the oscillations in the spectra of

astrophysical objects caused by the photon-ALP mixing (Batković et al. 2021). Since $P_{\gamma\gamma}$ depends on both the strength of the ALP-photon coupling and the intensity/coherence scale of the magnetic field, while our research focuses on the Perseus cluster, it is important to remember that there are many possible magnetic fields in the path of the photon. A complete study should consider a magnetic field on the local environment, on the galactic scale and on the intergalactic scale. Taking the example of AGN gamma rays from the AGN they would encounter:

- The strong magnetic fields of the cluster core and have a high chance of converting into ALPs.
- The weak magnetic field strength on the intergalactic level, with a moderate chance of converting in ALPs.
- The magnetic field in the Milky Way (MW), where ALPs could (or not) be reconverted into gamma rays.

These could all be possible imprints in the original gamma-ray spectrum. In a regime above the critical energy E_{crit} of eq. 3.17, where the photon–ALP mixing is maximum, if an ample fraction of photons is converted at the source into ALPs that do not later convert back in the MW, a signal depletion would be observed. Second case: if an ample conversion happens in the source but then a back conversion happens in the MW, an ampler signal than expected could be observed. The above signatures would be observed on top of the well-known gamma-ray extinction due to the interaction with the Extragalactic Background Light (EBL) (Horns et al. 2012; Angelis, Roncadelli, and Mansutti 2007) which strongly limits the observation of TeV emission above redshift $z \sim 1$. The propagation of VHE photons is affected by pair production processes with the EBL. Depending on the photon energy, there could be an interaction with the EBL or the cosmic microwave background (CMB), producing an electron–positron pair ($\gamma \rightarrow e^+ + e^-$). The flux attenuation caused by these processes is dominant for photon energies around $E_\gamma \approx 500$ GeV and $E_\gamma \approx 10^6$ GeV, respectively (Angelis, Roncadelli, and Mansutti 2007). Thus a great part of photons evades detection (because they get absorbed) and this means that the universe becomes opaque to VHE gamma rays. The above-mentioned cases of ALP signatures are possible. A third possible case happens at around E_{crit}. In this regime, the oscillatory behaviour in eq. 3.21 would create *wiggles* in the spectrum, in correspondence with the probability term. These wiggles would be hardly misinterpreted as being of astrophysical origin and would, therefore, constitute a clear detection (Sá nchez-Conde et al. 2009; Alessandro De Angelis, Galanti, and Roncadelli 2011; Hooper and Serpico 2007; A. De Angelis et al. 2009; Batković et al. 2021).

3.3 IACT

The Imaging Atmospheric Cherenkov Telescopes (IACT), are specially designed (or method) to detect very high energy (VHE) γ-ray photons in the energy range of $\sim$50 GeV to $\sim$50 TeV. They opened a new astronomical window to observe the γ-ray sky. Currently, there are four instruments: H.E.S.S.[1], MAGIC[2], FACT[3], and VERITAS[4]. The Cherenkov Telescope Array (CTA) is a multinational project to build next-generation IACTs.
The IACT uses one or more optical telescopes that image the air showers induced by cosmic γ-rays in the atmosphere through the *Cherenkov radiation* produced by the ultra-relativistic charged particles. The annihilation of positron and electron (e^+e^-) generates a ray of light that travels trough the medium at a speed higher than the phase velocity (Cherenkov effect). This faint light flash generally lasting just a few ns (10^{-9}s) can be detected by this special telescopes. Most of this light is emitted at altitudes ranging between 5 to 15 km. Above a few TeV, Cherenkov light from electromagnetic showers becomes significantly brighter, at the same time, the gamma-ray flux decreases with energy, so to detect a sufficient number of these high-energy events, a large ground surface needs to be covered.

3.4 MAGIC telescopes

MAGIC telescopes are a system of two 17 m diameter imaging atmospheric Cherenkov telescopes located at the Roque de los Muchachos Observatory (La Palma, Canary Island) at an altitude of 2200 a.s.l. The first telescope, MAGIC-I, is in operation since 2004. The second one, MAGIC-II, was built in 2008 at a distance of 85 m from the first. Both mirrors have a collecting area 236 m^2. They achieve the best performance for VHE gamma ray observation in the absence of moonlight. The two MAGIC telescopes can be operated independently or in stereoscopic mode, the second one allows a more precise reconstruction. Between 50 GeV and 150 GeV, MAGIC telescopes have the best sensitivity of the current IACT. MAGIC telescopes are a stereoscopic system of two IACTs, see fig. 3.3, it is one of the most sensitive currently operating instruments.
It is possible to identify the nature of the primary particle and reconstruct its original energy and incoming direction. These types of instruments work only at night and preferentially during dark moonless conditions. Therefore, the cameras of the MAGIC telescopes were designed from the beginning to allow observation during moderate moonlight (Ahnen 2017).

[1] High Energy Stereoscopic System.
[2] Major Atmospheric Gamma Imaging Cherenkov Telescopes.
[3] First G-APD Cherenkov Telescope.
[4] Very Energetic Radiation Imaging Telescope Array System.

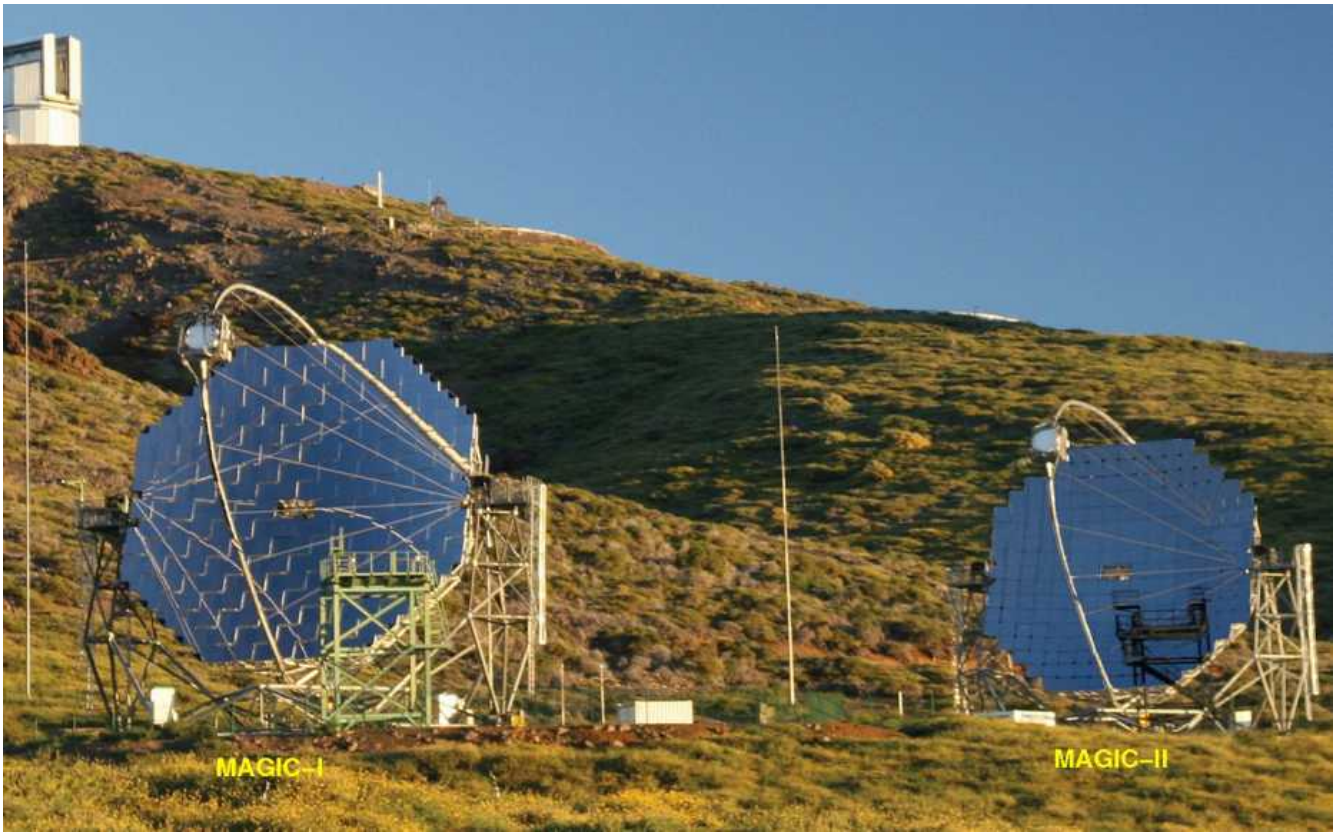

Figure 3.3: MAGIC telescopes, Roque de los Muchachos Observatory. On the left side MAGIC-I is active since 2004, on the right side MAGIC-II is active since 2009 to significantly increase the sensitivity by stereo observations. MAGIC are the largest of the current Cherenkov telescope systems. Both instruments are made up of individual mirror panels that can be independently focused using an active mirror control system equipped with lasers.

γ-rays of different origins have different spectral shapes. MAGIC is sensitive to cosmic γ-rays with photon energies between 50 GeV and 30 TeV, other ground-based γ-ray telescopes typically observe γ energies above 200–300 GeV. This means that MAGIC can cover an enormous energy spectrum (Bouvier 2011).

4. Application to the Perseus Cluster

4.1 The Perseus Cluster

The Perseus cluster, also known in literature as Abell 426, is a cluster of galaxies in the constellation Perseus with this characteristics:

- Recession speed v_{rec}=5366km/s.
- Diameter of 816'.
- Redshift z=0.0175 $\pm$ 0.0001.

It is one of the most massive objects in the known universe, containing thousands of galaxies immersed in a vast cloud of electronic gas, as mentioned before it is also the brightest cluster in the sky observed in the X-ray band.
It was first reported to be an extended source of X-rays from Uhuru[1] (1973) observations. The cluster has a prominent X-ray surface brightness peak centered on the active galaxy NGC 1275, containing a strong core-dominated radio source (Churazov et al. 2003). Another important object found inside the cluster is the galaxy IC 310, a head-tail radio galaxy that appears to be a strong a γ-ray source. Surveys within the 0.1° circle around the position of the γ-ray source have provided an unambiguous identification of the source with IC 310 (Neronov, Semikoz, and Vovk 2010).

IC310 is classified as a head-tail radio galaxy (also elliptical galaxy), it also presents blazar-like behaviour due to the strong AGN of the BL Lac-type object. It is thus expected that the γ-ray emissions are produced in the innermost part of the jet that is expelled by a supermassive black hole; however affirmations that the emission mechanism is the same cannot be made. Observational evidence however, did not detect the time variability typical of this objects, and the flux was consistent with the level measured during the past 10 yr by ASCA and ROSAT (Sato et al. 2005). An alternative possibility is that the γ-rays are produced at the bow shock formed in the interaction of the relativistic jet from the fast moving galaxy with the intracluster medium (Neronov, Semikoz, and Vovk 2010). Fermi data indicates that most of the γ-ray emission is produced in the *head* part of the source. At the same time, the Fermi angular resolution is not sufficient to distinguish between emission from the *head* of the bow shock and the emission from the base of the jet near the supermassive black hole, which powers the source's activity (Neronov, Semikoz, and Vovk 2010).
If the observed γ-ray emission is produced at the bow-shaped contact surface between the AGN outflow and the intracluster medium, the γ-ray emission should not be variable on timescales much shorter than $\sim 10^3$ yrs (Neronov, Semikoz, and Vovk 2010). No Variability of the γ-ray signal from IC 310 could be studied with Fermi, only five γ-rays from the source at energies above 30 GeV were detected (Neronov, Semikoz, and Vovk 2010). The five detected events did not come within a narrow time window (Neronov, Semikoz, and Vovk 2010), which would indicate the possibility of a strong flare from the source. The presence or the absence of variability of the VHE

[1] X-ray explorer satellite, first satellite launched specifically for X-ray astronomy.

γ-ray emission from IC 310 could be readily verified in the observations with ground based γ-ray telescopes. A previous observation of the region around Perseus cluster with Whipple telescope[2] has resulted in an upper limit one the source flux (Perkins et al. 2006). However, this upper limit is comparable to the Fermi measurement of the source flux, so that no conclusion about the presence or absence of long-term variability of the source could be drawn from the comparison of Whipple and Fermi observations. It is clear that observations of the source with more modern ground-based γ-ray telescopes MAGIC, would give much higher signal statistic at energies above 100 GeV, so that the hypothesis of the flux variability could be easily tested (Aleksi'c et al. 2014).
The sky-map of the cluster, shown in fig. 4.1, includes the radio galaxy NGC 1265. This source is identified in the radio band, but in contrary to IC 310, does not show significant X-ray and VHE γ-ray emission (Hildebrand 2012). A comparison of the physical parameters of IC 310 and NGC 1265, e.g. velocity through the intracluster medium, overall power of relativistic outflow etc., could help to clarify the conditions under which particle acceleration and VHE γ-ray emission in this type of sources occurs.

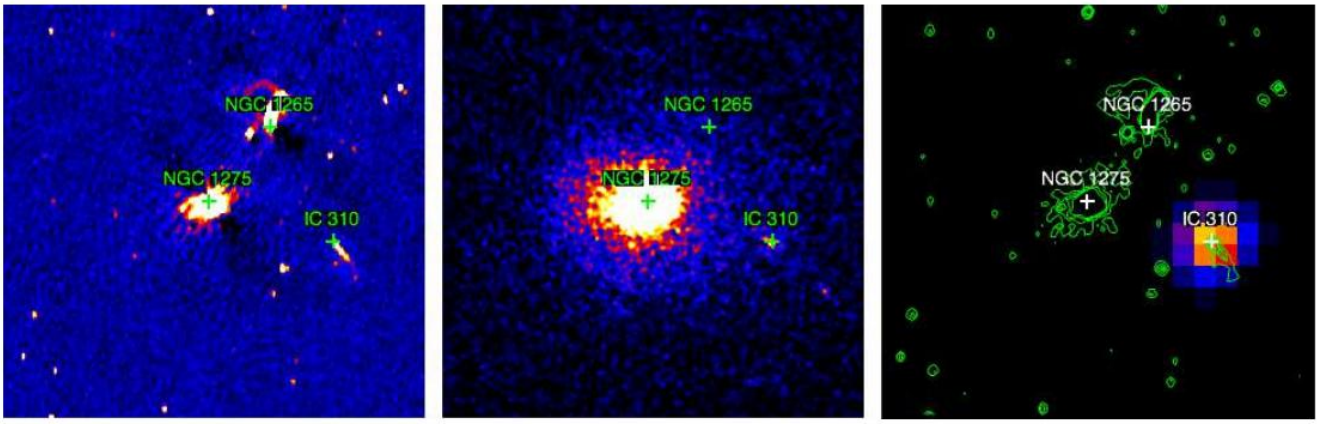

Figure 4.1: Image of Perseus galaxy cluster in radio band from WENSS sky survey (left), in the X-ray band from the ROSAT all-sky survey (middle) and the Fermi image in the 100-300 GeV energy band (right). The green contours on the right panel correspond to the radio image from the left panel (Neronov, Semikoz, and Vovk 2010).

[2] an American astronomical observatory owned and operated by the Smithsonian Astrophysical Observatory.

4.2 General Overview of the Perseus Cluster

The core of the Perseus Cluster was observed with XMM-Newton on 30 January 2001 with a total integration time of ∼53 ks, this observation gives access to a good view on the central parts of the cluster ∼Mpc (Churazov et al. 2003). The pointing was centered on NGC 1275. Subsequent analysis and results that we will bring here were done by previous work (Churazov et al. 2003).

Electron Density profile

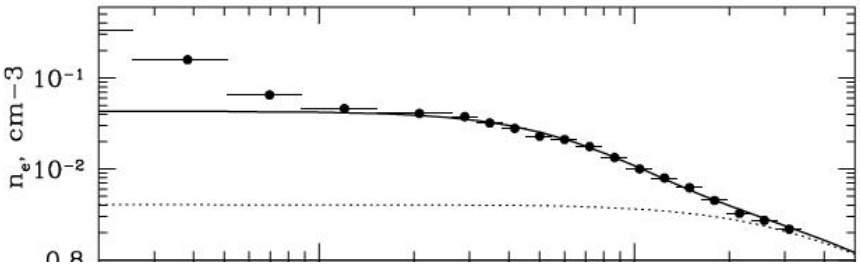

Figure 4.2: Radial profile of the electron density of the Perseus Cluster (Churazov et al. 2003).

The points are the values during the observations, the line is a general fit given by the formula (Churazov et al. 2003):

$$n_e = \frac{3.9 \times 10^{-2}}{[1+(\frac{r}{80})^2]^{1.8}} + \frac{4.05 \times 10^{-3}}{[1+(\frac{r}{280})^2]^{2.8}}. \tag{4.1}$$

Where r is the projected distance from the center of the cluster. We have also tried to fit the results with a more classical β-profile (Arnaud, M. 2009) eq. 2.41:

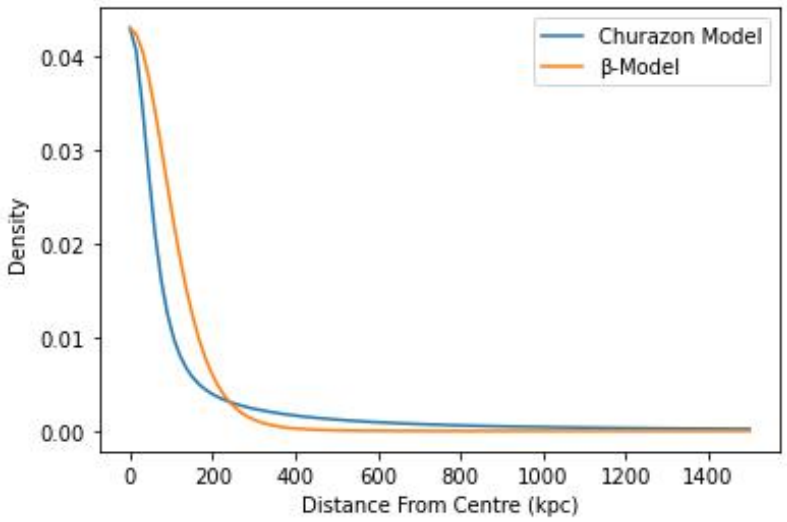

Figure 4.3: β-profile modelling for electron density eq. 2.41 for the Perseus Cluster.

Also the value of the core radius of the electronic density needed for the β-profile is given at r_c=250 kpc (Churazov et al. 2003).

Temperature profile

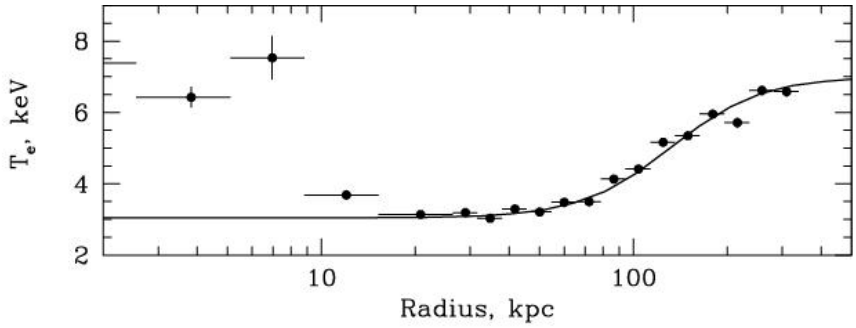

Figure 4.4: Radial profile of the temperature in the Perseus cluster (Churazov et al. 2003).

Again, the points are the values obtained through the observation, the line is a general fit approximation given by the formula (Churazov et al. 2003):

$$T = 7\frac{1+(\frac{r}{100})^3}{2.3+(\frac{r}{100})^3} \quad \text{keV}. \tag{4.2}$$

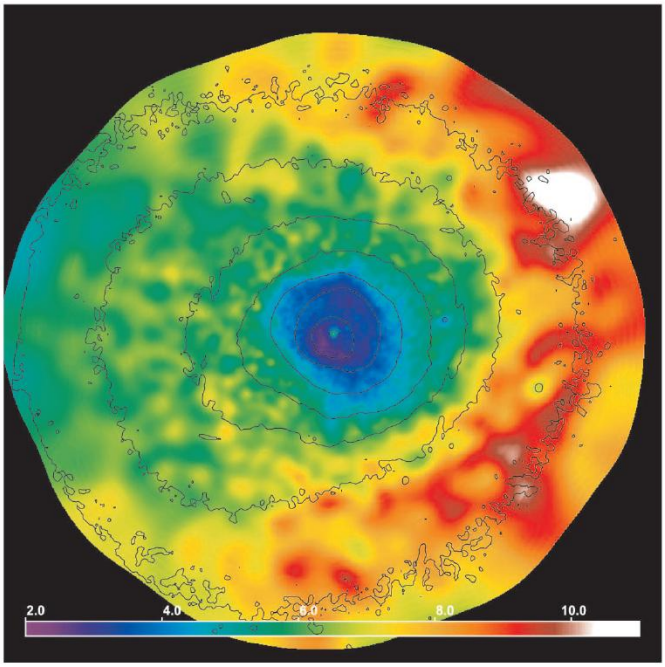

Figure 4.5: Gas temperature map of the Perseus Cluster ($30' \times 30'$), the countours rappresent the surface brightness distribution (Churazov et al. 2003).

Density Distribution of galaxies

The projected distribution of galaxies in the cluster was determined by counting galaxies on the Palomar Sky Survey plates in a set of 15 concentric circular rings centered on the cluster center. Each one of the rings was of equal width, 4 mm = 4'48 each. The counting was performed to two limiting magnitudes estimated at M $<$ 16.0 mag and M $<$ 17.5 mag (Bahcall 1974). Data is here presented:

		$P \lesssim 16.0$ mag		$P \lesssim 17.5$ mag	
RING*	$\bar{r}$ (arc min)	No. of Galaxies in Ring	ρ_{tot} (galaxies per square deg)	No. of Galaxies in Ring	ρ_{tot} (galaxies per square deg)
1	3.0	5	285	10	571
2	7.0	9	171	20	380
3	11.4	9	103	21	240
4	15.8	8	65	18	147
5	20.2	5	32	18	114
6	24.7	7	36	18	93
7	29.1	3	13	14	61
8	33.6	5	19	19	72
9	38.1			11	37
10	42.6	10	7.1	14	42
11	47.0			15	41
12	51.5			18	45
13	56.0			19	43
14	60.5	8	5.7	17	36
15	65.0			19	37

Figure 4.6: Data for the density distribution of galaxies in the Perseus Cluster (Bahcall 1974).

We have then fitted the set of data with both a polinomial curve and a formula proposed in previous work (Jaffe 1980;Govoni 2018):

$$n_g = n_{g_0}\left[1+\left(\frac{r}{r_{cg}}\right)^2\right]^{-\frac{3}{2}}. \tag{4.3}$$

Where n_{g_0} is the central density of the galaxy distribution and r_cg is the core radius of the galaxy density distribution measured at r_{cg}=178 kpc (Bahcall 1974).

The results can be seen in fig. 4.7 and 4.8:

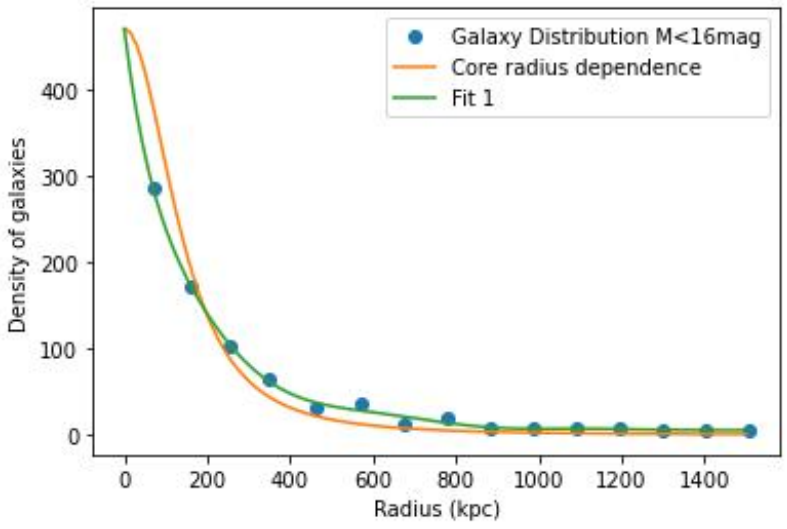

Figure 4.7: Fit for the density distribution of galaxies in the Perseus cluster M $<$ 16 mag (Bahcall 1974).

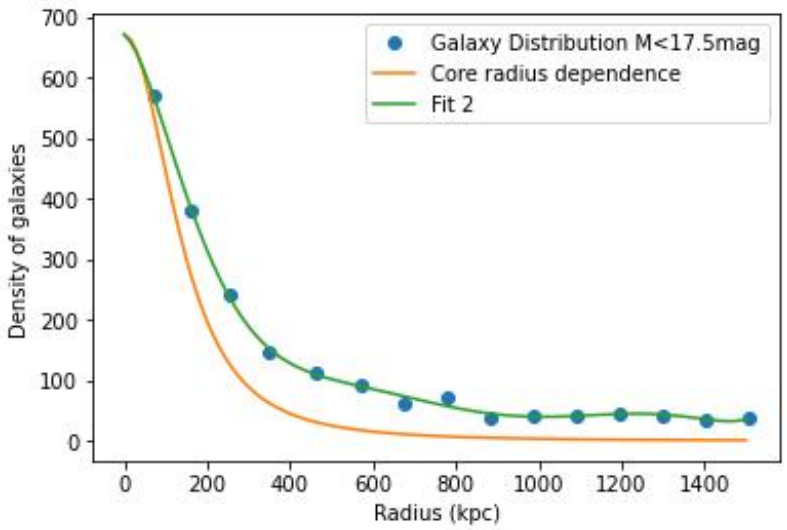

Figure 4.8: Fit for the density distribution of the galaxies in the Perseus cluster M $<$ 17.5 mag (Bahcall 1974).

4.3 Magnetic Field

4.3.1 Magnetic Field at the centre of the cluster (NGC1275)

Rotation Measure and Thermal Pressure

As stated in eq. 2.49, for a refractive medium in the presence of magnetic fields the polarization angle χ varies. The RM is related to the electron density n_e and the net line of sight of the magnetic field in the environment, as discussed in eq. 2.37. The central electron density n_e is 0.3-0.4 cm^{-3} (Carilli and Taylor 2002). By assuming the path length of 2 kpc, which probes the highest density gas in the cluster, and is also the typical dimension for RM paths in cooling core clusters (Carilli and Taylor 2002). Assuming a constant magnetic field orientation, the magnetic field strength of 15 μG has been found (Taylor et al. 2006). This is the component along the line-of-sight, so correcting by a factor of $\sqrt{3}$ (by assuming spherical symmetry of the field), a field strength of 25 μG is obtained. Field strength calculated with these parameters can be compared to the strength of a magnetic field that has the same pressure as a gas of the same electron density n$_e$ and the temperature of 3.5-5 $\times 10^7$ K using

$$\frac{B^2}{8\pi} = 2n_e kT. \tag{4.4}$$

In the central ($r < 2$ kpc) region of the Perseus cluster this gives B = 300 μG, so the magnetic pressure from the estimated B-field strength of 25 μG is in the 10-20% range of magnitude of the thermal pressure ($\sim 4 \times 10^{-9}$ dyn cm^{-2}). This result is similar to those found in other cooling core clusters, sec. 2.8. The RMs in NGC1275 in the ICM have an observed gradient of 10% on the RM on scales of $\sim$ 1 pc which is hard to reconcile with fields organized on kpc scales (Taylor et al. 2006).

Mathematical Simulation

In the center of the Perseus cluster, like in many other clusters containing a active galaxy, an X-ray cavity was observed, spatially coinciding with the a radio mini-halo (Schmidt, Fabian, and Sanders 2002; Sanders, Fabian, and Dunn 2005). This cavity most probably is a result of the interaction between outflows of NGC 1275 and the intracluster gas. The X-ray cavity size, according to Chandra observations (Sanders, Fabian, and Dunn 2005), is 93 kpc, while the radio mini-halo extends slightly further. As discussed in sec. 2.8, the slashing cold front in the Perseus cluster, indicates that the X-ray cavity should be filled with relatively high magnetic field in order to support the required pressure. This magnetic field region is seen on the RM map of the Perseus cluster (Brentjens and Bruyn 2005) and explains high values of the rotation measure observed in for the very center of the cluster. For the X-ray cavities, blown by radio-galaxy jets in the intracluster plasma, magnetic fields are expected to be regular at large scales (Gourgouliatos, Braithwaite, and Lyutikov 2010). A model with the consistent magnetic field solution has been used (Libanov and Troitsky 2020):

$$B_r = 2\cos\theta \frac{f(r_1)}{r_1^2} \tag{4.5}$$

$$B_\theta = -2\sin\theta \frac{f'(r_1)}{r_1} \tag{4.6}$$

$$B_\phi = 2\alpha\sin\theta \frac{f(r_1)}{r_1} \tag{4.7}$$

Where f is the function (with f' being its derivative) :

$$f = C(\alpha\sin(\alpha r_1) - \frac{\sin(\alpha r_1)}{r_1} - \frac{F_0 r_1^2}{\alpha^2} \tag{4.8}$$

$$F_0 = C\alpha^2(\alpha\cos\alpha - \sin\alpha) \tag{4.9}$$

Where α is the lowest non-zero root of:

$$\tan\alpha = \frac{\alpha}{3-\alpha^2}. \tag{4.10}$$

B_r, B_θ, B_ϕ indicate the various components of the magnetic field, $r_1 = r/R$ where R is the cavity radius and r the projected distance from the centre and C is the normalization constant determined by the field value at $r = 0$. This analytical solution is supported by numerical simulations in (Libanov and Troitsky 2020), assuming the viewing angle $\theta = 45^\circ$ and the cavity radius stated above. The normalization of the field is chosen in such a way that the Faraday RM of ~ 7300 rad$\cdot$ m^{-2} (Taylor et al. 2006) for the central direction is reproduced for the electron density derived from X-ray observations (Churazov et al. 2003). This normalization gives the total field strength in the center of 8.3 μG. The field components for the chosen line of sight are plotted in fig. 4.9. It should be noted that the central X-ray cavity may not be the only place in the Perseus cluster where fields ordered at large scales equally organised structures on the $\sim$Mpc scales should be discussed, possibly associated with a shock caused by the interaction of the intracluster matter with intergalactic matter in the large-scale structure filament, which may or may not be similar to the regular field structures observed in other galaxy clusters with similar conditions. In addition, X-ray observations reveal (Churazov et al. 2003) large-scale (> 100 kpc) spiral structure around NGC 1275, which also may host regular magnetic fields, like it happens in our Galaxy. Thus meaning that the structure of regular magnetic fields in the Perseus cluster is rich and unknown, lacking explicit measurements.

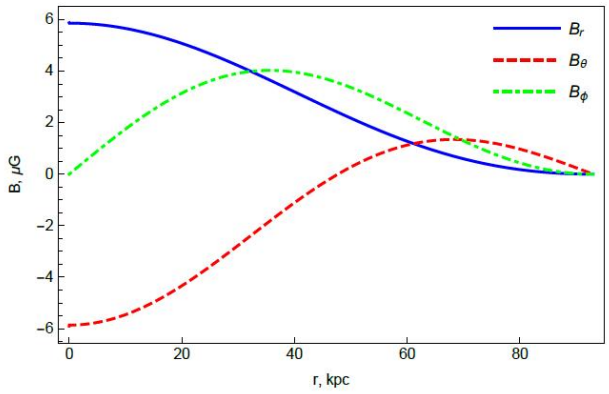

Figure 4.9: The longitudinal direction of the magnetic field B_r, and the two transverse directions B_θ and B_ϕ, components for the solution for the X-ray cavity around NGC 1275 (Libanov and Troitsky 2020).

4.3.2 Magnetic Field at the position of IC310

Inverse Compton Radiation

The X-ray radial profile of IC 310 is well fitted by the PSF of a point source. The energy spectrum was fitted with an power-law model with a rather steep photon index of 2.5. These features are possible indication (like we already discussed in sec. 4.1) that the emission of IC 310 originates from the central AGN of the BL Lac-type object. Estimation were made of the possible X-ray emission from hot interstellar medium (Yamasaki, Ohashi, and Furusho 2002) based on the L_X-L_B relation for elliptical galaxies. The optical luminosity of IC 310 was shown to be $L_B \sim 10^{10}$ $L_\odot$. This corresponds to an X-ray halo luminosity of $L_X \sim 10^{39}$ erg s^{-1}, which is three orders of magnitude lower than that of the observed IC 310 value. This indicates that the X-ray emission of IC 310 is dominated by the AGN component, and the halo emission, if present at all, is masked by the PSF of the strong point-source emission. With much higher angular or spectral resolution, one may be able to detect the X-ray emission from a hot-halo associated with this galaxy. VLA observations indicate a radio lobe in IC310, and the radio flux densities at 49 cm, S_{49cm}, are reported to be about 1.3 Jy (Bruyn and Brentjens 2005). The radio halo, whose size is $15' \times 4'$, was searched for any flux excess by comparing the flux with those in the immediate surrounding region. No significant excess in the X-ray flux from the radio lobe was detected (Sato et al. 2005); the upper limit is $F_X(0.5-10\text{keV}) < 6 \times 10^{-14}$erg cm^{-2} s$-1$ $L_X(0.5-10\text{keV}) < 5 \times 10^{40}$erg s^{-1}. By assuming that the X-rays are emitted through the inverse Compton process with 2.7 K photons by the same relativistic electrons responsible for the radio lobe, the strength of the magnetic field is constrained. Following this study an inferior value of the magnetic field has been found $B \geq 1$ μG.

Faraday Depth

The observations of the Faraday Depth (FD) were done with the Westerbork Synthesis Radio Telescope (WSRT)[3]. Observations were conducted for 6×12 hours (Brentjens and Bruyn 2006). There were 126 usable frequency channels between 315 and 360 MHz. The theoretical noise limit, 50 μJy beam^{-1}. The noise level that achieved in the RM-cube (fig. 4.10) is about 70 μJy beam^{-1}rmtf^{-1}. This is much better than the classical confusion noise of about 1.5 mJy beam^{-1} in Stokes I for this frequency and resolution. The image shows a frame from the RM-cube of the Perseus cluster and it's the image 4.10 with the deepest low frequency polarization radio map ever constructed. The grey scale is the total linearly polarized flux per unit of FD ϕ.

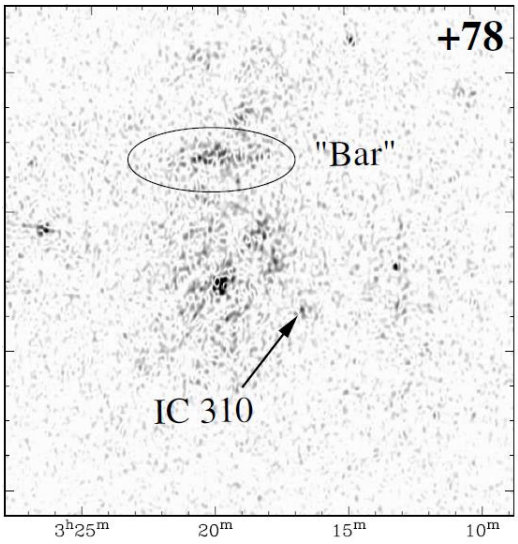

Figure 4.10: Characteristic frames from the RM-cube. The Faraday depth of the frame is specified in the top right corner in rad m^{-2}. The resolution of the image is $2' \times 3'$ (RA$\times$DEC) (Brentjens and Bruyn 2006).

A triangle of bright, extended sources dominates the field centre: NGC 1275 at the centre, the "Bar" at the top, and IC 310 at the lower right. IC310 shows up at $\phi \simeq +80$ rad m^{-2}. No significant emission at $\phi > 85$ rad m^{-2} has been seen. Considering that the shortest spacing was unavailable in several frequency bands, it is likely that the actual polarization percentage is a factor of 2–3 lower, making it high ($>$ 20-40%), but plausible. One can estimate a lower limit to the magnetic field in the cloud that performs the Faraday rotation. This cloud must be in front of polarized structures. We calculate the magnetic field with $|\Delta l| \simeq 2$ Mpc and n_e will be calculated through the various methods presented above. We also assume a constant, homogeneous magnetic field along the line of sight. Given an excess of order $+80$ rad $\cdot$m^{-2}, we can estimate:

$$|B| \geq \frac{\phi}{n_e |\Delta l|}. \tag{4.11}$$

Being this only the line-of-sight component then we will correct this value by $\sqrt{3}$.
Inserting the data from 4.2 we obtain:

[3]The telescope is an East-West array of fourteen 25 m parabolic dishes. The maximum baseline is 3 km, yielding a resolution of $\simeq 1' \times 1.5'$ (RA$\times$DEC) at 90 cm wavelength.

- for 4.1 at the position of IC310 $n_e = 6.7 \times 10^{-4} \pm 10^{-5}$ giving $|B| \geq 0.12 \pm 0.01$ μG ,
- for 2.41 at the position of IC310 $n_e = 4.4 \times 10^{-4} \pm 10^{-5}$ giving $|B| \geq 0.19 \pm 0.01$ μG.

This is a lower limit. In reality, the magnetic field is probably somewhat tangled, so it may not point directly towards us. Furthermore, the line of sight may be considerably shorter than 2 Mpc.

4.3.3 Magnetic Profile

σ_{RM}-S_x Relation

Important clues on the magnetic field distribution can be derived from Magnetohydrodynamics (MHD) cosmological simulations (Klaus Dolag, Matthias Bartelmann, and Harald Lesch 2002; K. Dolag, M. Bartelmann, and H. Lesch 2002). The formation of magnetized galaxy clusters from an initial density perturbation field was simulated, using a cosmological MHD code. A μG level field presently observed in clusters can be reproduced by the evolution of the magnetic field starting from an initial field of strength $\sim 10^{-9}$ G at redshift z = 15 (Klaus Dolag, Matthias Bartelmann, and Harald Lesch 2002). This field is amplified by compression during the cluster collapse. They obtained that the process of large-scale structure formation in the universe drives the characteristics of these magnetic fields. One of their results is that the magnetic field strength at any point within galaxy clusters is proportional to the gas density. In the simple case of adiabatic compression during a spherical collapse due to gravity, the field lines are frozen into the plasma, and compression of the plasma results in compression of flux lines. The expected growth of the magnetic field is roughly proportional to the gas density as $B \propto \rho^{\frac{2}{3}}$ (Govoni 2018), as a consequence of the magnetic flux conservation. From the simulations, predictions of the existence of a correlation between the Faraday rotation measure and the X-ray flux have been made (K. Dolag, Schindler, et al. 2001), finding that σ_{RM} increases with the X-ray flux:

$$\sigma_{RM} \propto S_x^f \tag{4.12}$$

with $f \simeq 1$. Some results of this study are presented in fig. 4.11. The data points are marked with different grey scale levels according to the individual cluster temperature. Theoretical predictions are shown as lines for three temperatures. Data points for different sources in the same cluster follow very well the predicted lines. The simulations also predict these lines to be shifted according to the temperature of the cluster. This trend is also confirmed by the data points:

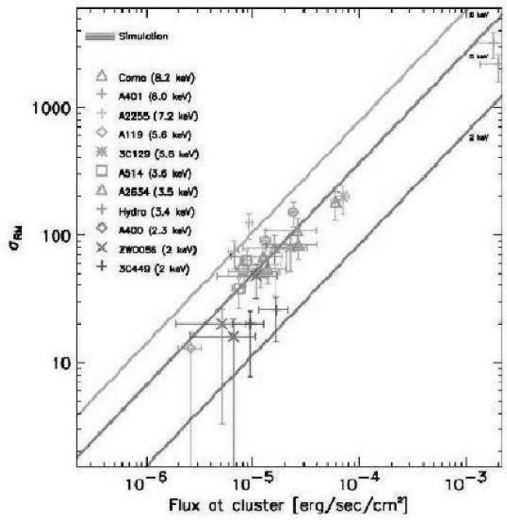

Figure 4.11: The correlation between the observed σ_{RM} and the X-Ray flux, and comparison with theoretical predictions in various clusters.

The X-ray surface brightness can be written as (Govoni 2018):

$$S_x \propto \int n_e^2 \sqrt{T} dl. \tag{4.13}$$

The RM dispersion, obtained from eq. 2.40, is related to B and n_e. The two observables σ_{RM} and S_x relate the two line of sight integrals with each other, therefore in comparing these two quantities, the cluster magnetic field and the thermal density are being compared. Thus the magnetic field profile can be represented by:

$$B(r) \propto B(0) \left(\frac{n_e(r)}{n_e(0)} \right)^{\eta}. \tag{4.14}$$

In the particular case of the β-model 2.41, the X-ray flux S_x is:

$$S_x \propto \left(1 + \frac{r_\perp^2}{r_c^2} \right)^{-3\beta + \frac{1}{2}}. \tag{4.15}$$

By substituting eq. 4.14 in the expression of σ_{RM} derived from eq .2.40, the following equation is obtained:

$$\sigma_{RM} \propto \left(1 + \frac{r_\perp^2}{r_c^2} \right)^{-3\beta(1+\eta) + \frac{1}{4}}. \tag{4.16}$$

Thus, by comparing S_x and σ_{RM}, one finds that the index η is related to the slope f and to the parameter β, through:

$$\eta = \frac{1}{\beta}(2f - 1)\left(\beta - \frac{1}{6}\right). \tag{4.17}$$

It can be seen that for a constant magnetic field ($\eta = 0$) the slope of the σ_{RM}-S_x correlation should be $f = 0.5$ while a steeper slope would imply $\eta > 0$. Various simulations for this relation can be seen in fig. 4.11.

For the nearby cluster A119 (z = 0.0442) one of the most studied clusters, the polarization properties of 3 extended radio galaxies have been studied (Govoni 2018), through this studies with have established that the σ_{RM}-S_x relation yields $B \propto n_e^{\eta}$ with η= 0.9. The most common values in literature for η are η=0.5, $\frac{2}{3}$,0.9, and here

we present results from various values of η since no exact study of the σ_{RM}-S_x has been done. These simulations will be applied both to the possible β-model for the cluster and to the density model present. The different values proposed in sec. 4.3.1 for the central magnetic field will be computed here with a middle-ground value of 15 μG. The simulations predict not only that the magnetic field scales similarly to the density within all clusters, but also that clusters should have different central magnetic field strengths depending on their temperature and therefore their mass.

The values we obtain are:

- For 4.1 at the position of IC310 $n_e = 6.7 \times 10^{-4} \pm 10^{-5}$ cm^{-3} :
  - For $\eta = 0.5$
    - $B = 1.04 \pm 0.04$ μG for B_0=8.3 μG
    - $B = 1.87 \pm 0.07$ μG for B_0=15 μG
    - $B = 3.11 \pm 0.13$ μG for B_0=25 μG
  - For $\eta = \frac{2}{3}$,
    - $B = 0.51 \pm 0.02$ μG for B_0=8.3 μG
    - $B = 0.93 \pm 0.05$ μG for B_0=15 μG
    - $B = 1.55 \pm 0.08$ μG for B_0=25 μG
  - For $\eta = 0.9$,
    - $B = 0.19 \pm 0.01$ μG for B_0=8.3 μG
    - $B = 0.35 \pm 0.02$ μG for B_0=15 μG
    - $B = 0.59 \pm 0.04$ μG for B_0=25 μG
- For eq. 2.41 at the position of IC310 $n_e = 4.4 \times 10^{-4} \pm 10^{-5}$ cm^{-3}:
  - For $\eta = 0.5$:
    - $B = 0.83 \pm 0.04$ μG for B_0=8.3 μG
    - $B = 1.51 \pm 0.07$ μG for B_0=15 μG
    - $B = 2.52 \pm 0.09$ μG for B_0=25 μG
  - For eq. $\eta = \frac{2}{3}$,
    - $B = 0.39 \pm 0.02$ μG for B_0=8.3 μG
    - $B = 0.70 \pm 0.05$ μG for B_0=15 μG
    - $B = 1.17 \pm 0.08$ μG for B_0=25 μG
  - For $\eta = 0.9$,
    - $B = 0.13 \pm 0.01$ μG for B_0=8.3 μG
    - $B = 0.24 \pm 0.02$ μG for B_0=15 μG
    - $B = 0.40 \pm 0.04$ μG for B_0=25 μG

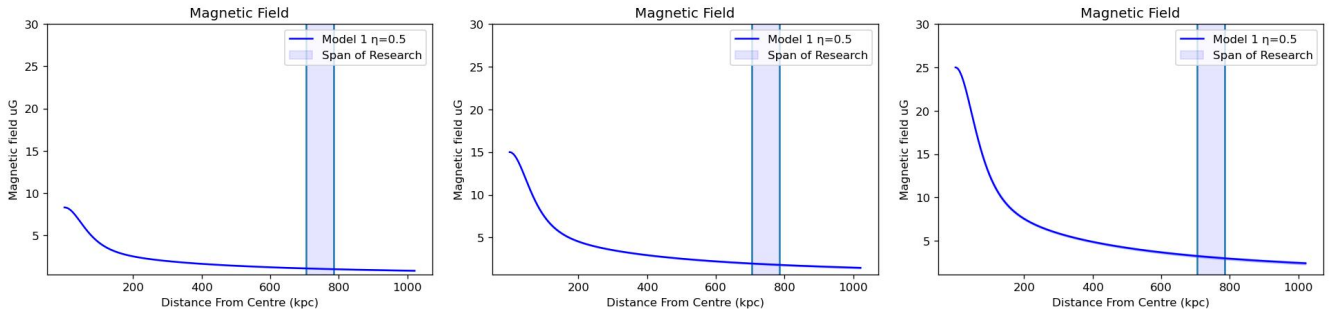

Figure 4.12: Various possible models for the 4.1 density model in the Perseus cluster with $\eta = 0.5$. The image at the top has a central magnetic field strenght of B=8.3 μG, for the central image the central field strenght is B=15 μG and at the bottom B=25 μG. Highlighted in blue the possible location of IC310.

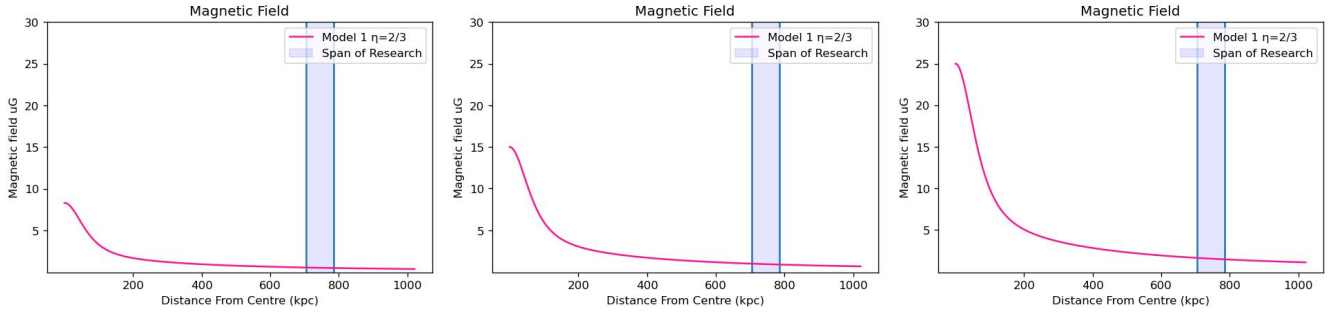

Figure 4.13: Various possible models for the 4.1 density model with $\eta = \frac{2}{3}$.The image at the top has a central magnetic field strenght of B=8.3 μG, for the central image the central field strenght is B=15 μG and at the bottom B=25 μG. Highlighted in blue the possible location of IC310.

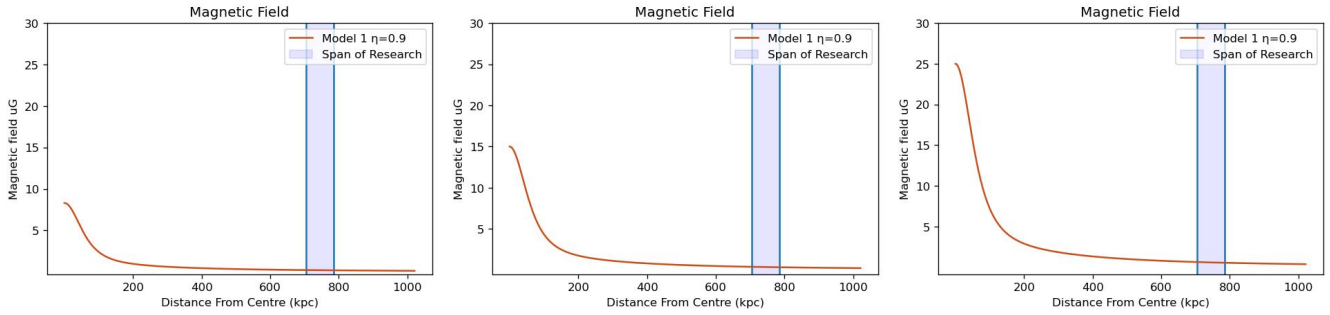

Figure 4.14: Various possible models for the 4.1 density model with $\eta = 0.9$. The image at the top has a central magnetic field strenght of B=8.3 μG, for the central image the central field strenght is B=15 μG and at the bottom B=25 μG. Highlighted in blue the possible location of IC310.

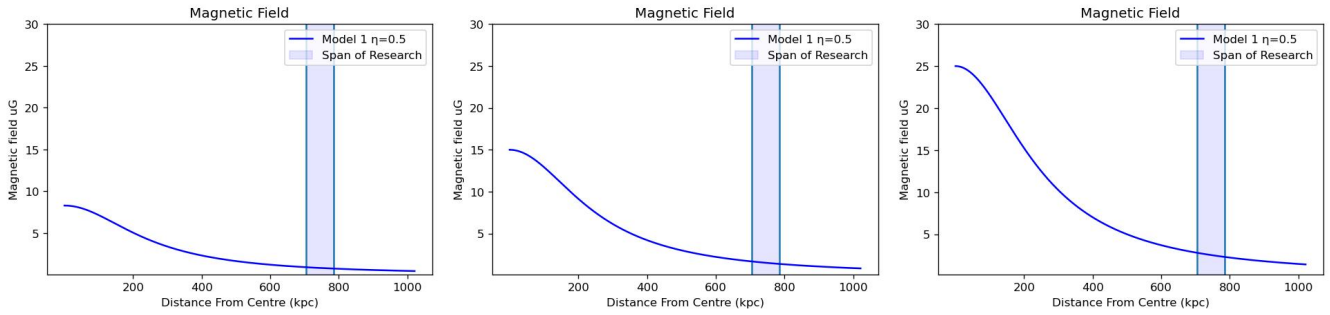

Figure 4.15: Various possible models for the 2.41 density model with $\eta = 0.5$. The image at the top has a central magnetic field strenght of B=8.3 μG, for the central image the central field strenght is B=15 μG and at the bottom B=25 μG. Highlighted in blue the possible location of IC310.

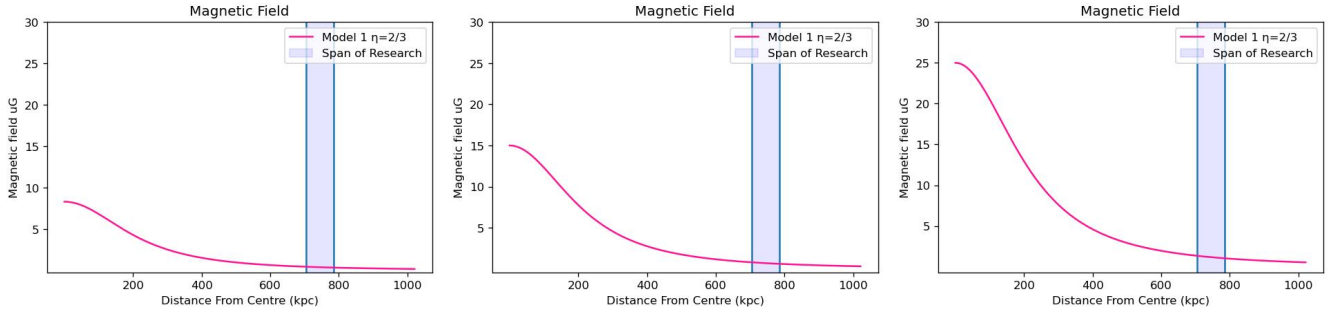

Figure 4.16: Various possible models for the 4.1 density model with $\eta = \frac{2}{3}$. The image at the top has a central magnetic field strenght of B=8.3 μG, for the central image the central field strenght is B=15 μG and at the bottom B=25 μG. Highlighted in blue the possible location of IC310.

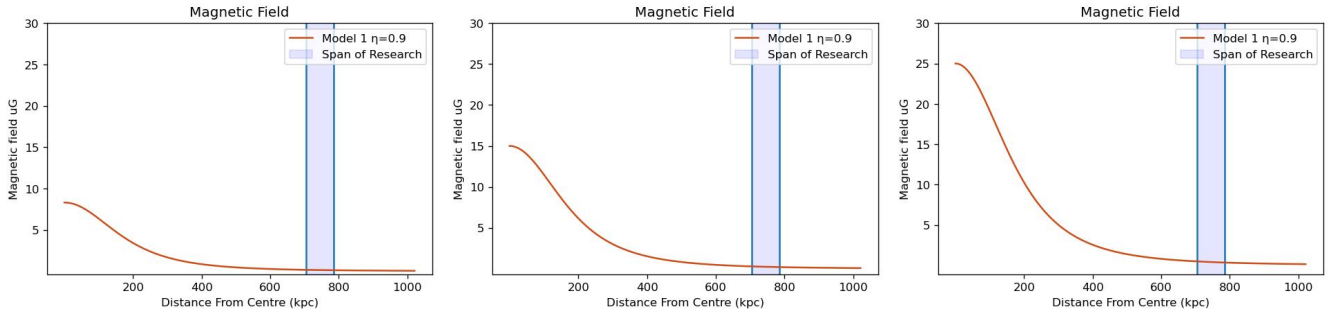

Figure 4.17: Various possible models for the 4.1 density model with $\eta = 0.9$. The image at the top has a central magnetic field strenght of B=8.3 μG, for the central image the central field strenght is B=15 μG and at the bottom B=25 μG. Highlighted in blue the possible location of IC310.

Turbulence Theory

The GC move trans-sonically through the intracluster medium. The following reasoning is made by assuming that the galaxies act as blunt objects with a characteristic radius a and that the medium behaves as a fluid with large Reynolds number. The galaxy will then have multiple weak bow and tail shocks and a turbulent wake (Jaffe 1980). The shocks and the wake will each dissipate power $P_0 \simeq \frac{1}{2} n_e v_g^3 \pi^2$, where n_e is the ICM electron density and v_g is the galaxy velocity. It has been argued (Jaffe 1980) that the viscosity of the medium might be very large and the Reynolds number correspondingly small, in which case there might be no turbulent wakes. This, however, was found using the Coulomb cross section to evaluate the particle mean free path s, which was found to be in the order of 100 kpc. This seems a gross oversimplification, since even at the lowest acceptable field strengths particle trajectories are completely dominated by the magnetic field (Jaffe 1980). In this case, except for very special geometries, mean free paths and kinetic viscosities are smaller by factors of order $(s/r_l)^2$, where r_l is the Larmor radious $\simeq 10^{10}$ cm (Spitzer 1956). The chief unknown in the above estimate of P_0 is the effective radius a. The gravitational interaction between the galaxy and the medium suggests a minimum value of a to be given by the accretion radius $r_a = GM/v_g^2$. Finally, if a galaxy loses interstellar material in the form of a wind, the pressure of this wind P_W will open a cavity about the galaxy of a radius given by:

$$P_W \simeq \dot{M} \frac{v_{wind}}{(4\pi r_w^2)} \simeq n_e v_g^2. \tag{4.18}$$

Then:

$$r_W \simeq \left(\frac{M v_{wind}}{4\pi n_e v_g^2} \right)^{\frac{1}{2}}. \tag{4.19}$$

Characteristic velocities and scales in the wake by using dimensional arguments need to be traced, like those in the Kolmogorov theory of turbulence. Near the head of the wake the scale of the largest vortices is of the order of the radius of the wake, a, and the turbulent velocity on the largest scale, v_t, is of order v_g. Behind the head, the wake spreads, and the disturbances slow down both from geometric spreading and from the dissipative conversion of the kinetic energy into heat. Without dissipation, the turbulent energy per unit length in the wake would be constant. By denoting this quantity as $W(x)$; it has the initial value P_0/v_g. The distance along the wake is designated as x and the turbulent energy density in the wake as $U(x)$. By then making the dimensional arguments that the wake spreads in the transverse direction at a velocity of order v_t(x); that the scale of the largest vortex is approximately the wake radius $r(x)$, and that the energy is dissipated on a characteristic time scale of $\frac{r(x)}{v_t(x)}$. The following relations hold now:

$$W(x) \simeq U(x) r^2(x) \simeq n_e v_t^2 r^2 \tag{4.20}$$

$$\frac{dr}{dx} \simeq \frac{v_t(x)}{v_g} \tag{4.21}$$

$$\frac{dW}{dx} \simeq \frac{1}{v_g} \frac{dW}{dt} \simeq \frac{W v_t}{(r v_g)} \tag{4.22}$$

which we can solve, and they give:

$$W(x) \simeq W_0 (\frac{x}{a})^{-\frac{2}{3}} \tag{4.23}$$

$$r(x) \simeq a (\frac{x}{a})^{\frac{1}{3}} \tag{4.24}$$

$$v_t(x) \simeq v_g(\frac{x}{a})^{-\frac{2}{3}} \tag{4.25}$$

At a certain distance x_A, when $r = r_A$, the local turbulent velocity $v_t(x_A)$ falls below the general Alfvén speed in the cluster, v_A (Jaffe 1980), and the wake will change character, becoming a group of Alfvén waves with maximum wavelength of order r_A and spreading with constant velocity v_A, until it merges with the wakes of other galaxies. Simple algebra shows:

$$x_a \simeq a(\frac{v_g}{v_a})^{\frac{3}{2}} \tag{4.26}$$

$$r_A \simeq a(\frac{v_g}{v_a})^{\frac{1}{2}} \tag{4.27}$$

$$W_A = W_0(\frac{v_A}{v_g}). \tag{4.28}$$

In the post-Alfvénic wake dissipation arises primarily from nonlinear mode coupling of the Alfvén waves. The characteristic time for this process is:

$$\tau \sim \frac{b_t}{\dot{b_t}} \sim (\frac{b_0^2}{b_t^2})\frac{r_A}{v_A}. \tag{4.29}$$

The notation $b = B/(4\pi n_e)^{\frac{1}{2}}$ has been used here so that b has units of velocity and b_0, the average field strength, equals v_A. The equations 4.20, 4.21, 4.22 can be replaced in the post-Alfvénic wake by:

$$W \simeq n_e b_t^2 r^2 \tag{4.30}$$

$$\frac{dr}{dx} \simeq v_A \tag{4.31}$$

$$\frac{dW}{dx} \simeq -\frac{W}{v_g \tau} \simeq (\frac{w}{v_g})(\frac{v_A}{r_A})(\frac{b_t^2 2}{v_A^2}). \tag{4.32}$$

These yield:

$$W \simeq W_A(2 - \frac{x}{x_A})^{-1}. \tag{4.33}$$

The numerical constants in this expression are uncertain by factors of order unity, but the expression shows that after the Alfvénic transition, but before merging, the energy density (proportional to W_r^{-2}) drops so quickly that the dissipation slows and the residual energy per unit length asymptotically approaches a constant of order:

$$W_\infty \sim (\frac{P_0}{2}) \times (\frac{v_A}{v_g^2}). \tag{4.34}$$

Merging occurs when the wakes fill the core volume. In the post-Alfvénic region

$$r \simeq x(\frac{v_a}{v_g}) \tag{4.35}$$

so the distance x_m at merging is given by:

$$x_m \simeq R_g(\frac{v_g}{v_A})^{\frac{2}{3}} N_g^{-\frac{1}{3}} \simeq (\frac{v_g}{v_A})^{\frac{2}{3}} n_g^{-\frac{1}{3}} \tag{4.36}$$

n_g is the central galaxy density. Then:

$$\frac{x_m}{x_A} \simeq \frac{r_m}{r_A} \simeq (\frac{v_g}{v_A})^{\frac{5}{3}} (n_g a^3)^{-\frac{1}{3}}. \tag{4.37}$$

Finally, the ratio of turbulent to large-scale field at merging is:

$$\frac{b_m}{v_A} = (\frac{r_m}{r_A})^{-2} \simeq (\frac{v_g}{v_A})^{\frac{5}{3}} (n_g a^3)^{\frac{2}{3}}. \tag{4.38}$$

The distinction between turbulent and general field is meaningful only if b_m<v_A, which occurs if:

$$\frac{v_g}{v_A} < (n_g a^3)^{-0.4}. \tag{4.39}$$

The model then forces us to conclude that most of the magnetic energy in the cluster core has been turbulently generated. No wave energy loss by propagation out of the core was assumed. This can be justified a posteriori by comparing the power dissipation for turbulent turnover, which is proportional to (v_A/r_A), to the power leaving the core by propagation, which is proportional to (v_a/R_c). Dissipative losses exceed propagation losses by a factor of R_c/r_A, which is of order $\sim$10. A similar calculation shows that propagation is also negligible in the outer parts of the cluster, allowing straightforward calculation of the dependence of the field strength on distance from the cluster center since:

$$v_a \propto (n_g a^3)^{0.4} \tag{4.40}$$

which finally gives our magnetic field profile profile:

$$B(n_e, n_g) \propto B(0)(\frac{n_g}{n_{g0}})^{0.4} (\frac{n_e}{n_{e0}})^{0.5} \tag{4.41}$$

where $B(0)$ is the central magnetic field intensity, n_g is the density of galaxies, n_{g0} is the central density of galaxies, n_e is the gas density, and n_{e0} is the central gas density. If we now apply the common β-model eq. 2.41 to the gas density and we use eq. 4.3 for the density of galaxies, we have another expression:

$$B(R) \propto B(0)(1 + (\frac{R}{R_c})^2)^{-0.75\beta} (1 + (\frac{R}{R_g})^2)^{-0.6} \tag{4.42}$$

where R is the distance from the center, R_c is the core radius of the gas density, and R_g is the core radius of the galaxies distribution. Here are given the results:

- For 4.1 at the position of IC310 $n_e = 6.7 \times 10^{-4} \pm 10^{-5}$ cm^{-3} .
  - For the polinomial fitting that considers only galaxies with $M \leq 16$ mag we obtain:
    - $B = 0.26 \pm 0.01$ μG for B_0=8.3 μG
    - $B = 0.48 \pm 0.02$ μG for B_0=15 μG
    - $B = 0.81 \pm 0.03$ μG for B_0=25 μG
  - For the polinomial fitting that considers even galaxies with $M \leq 17.5$ mag we obtain:
    - $B = 0.40 \pm 0.01$ μG for B_0=8.3 μG
    - $B = 0.72 \pm 0.03$ μG for B_0=15 μG
    - $B = 1.20 \pm 0.05$ μG for B_0=25 μG

- For eq. 4.42 at the position of IC310 we obtain:
  - $B = 0.55 \pm 0.01$ μG for B_0=8.3 μG
  - $B = 1.01 \pm 0.01$ μG for B_0=15 μG
  - $B = 1.68 \pm 0.01$ μG for B_0=25 μG.

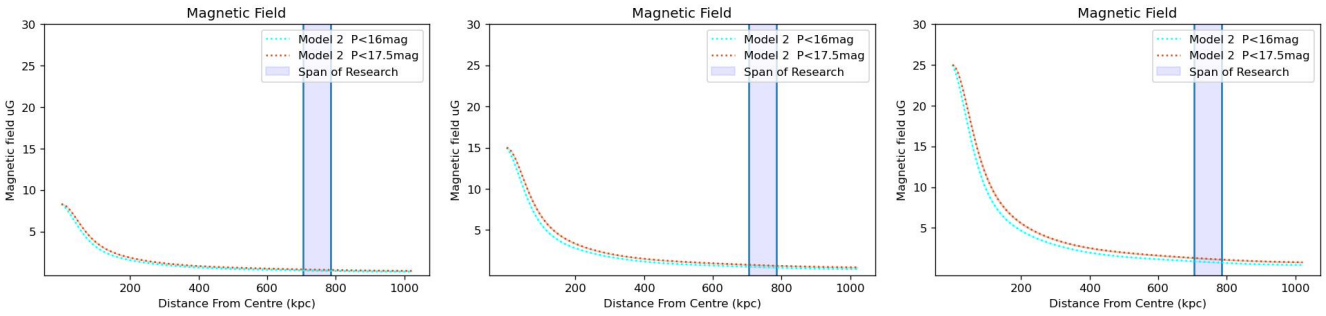

Figure 4.18: Various possible models for the two polinomial fittings of the density model and density model 4.1 on the top the central magnetic field value is B =8.3 μG, for the central B =15 μG at the bottom B =25 μG highlighted in blue the possible location of IC310.

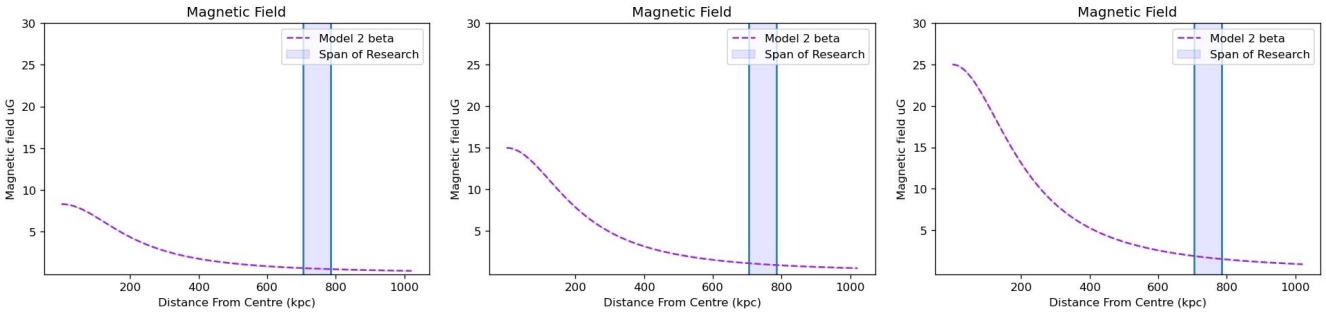

Figure 4.19: Various possible models for 4.42 on the top the central magnetic field value is B =8.3 μG, for the central B =15 μG at the bottom B =25 μG highlighted in blue the possible location of IC310.

4.4 Discussion

From the results presented in the previous section sec. 4.3.1, it is derived that cluster magnetic field strengths obtained from the RM arguments (sec. 2.6 and 4.3.1) are about an order of magnitude higher than the estimates obtained from the mathematical model in X-ray cavity/mini-halo (sec. 2.2.1), this seems in line with what has been indicated as plausible in fig. 4.20.

Method	**Strength μG**	**Model parameters**
Synchrotron halos	0.4–1	Minimum energy, $k = \eta = 1$, $\nu_{low} = 10$ MHz, $\nu_{high} = 10$ GHz
Faraday rotation (embedded)	3–40	Cell size = 10 kpc
Faraday rotation (background)	1–10	Cell size = 10 kpc
Inverse Compton	0.2–1	$\alpha = -1$, $\gamma_{radio} \sim 18000$, $\gamma_{xray} \sim 5000$
Cold fronts	1–10	Amplification factor ~3
GZK	>0.3	AGN = site of origin for EeV CRs

Figure 4.20: Synthesis of possible values that can be obtained through various methods (Carilli 2002).

We can see that the RM values for the fields seems in line for what can be expected. This can be argued both in favor and against. As shown in Fig. 4.4 and Fig. 4.5 we can see how the radial profile in temperature is firstly a rough approximation made by assuming spherical symmetry that is an assumption far from what is actually present within the cluster, thus meaning that the error on the measurements of the density may be higher, (this same argument can be said about the density as seen in fig. 4.2). As the image would suggest the presence of a cold front enhancing the magnetic field 2.8 up to 25 μG could be an option to consider, although nothing can be said about for certain until further analysis. But even the presence of a cold front could not completely explain the value of the B-field in the center of the cluster the same method has been applied to the study of the Coma and the A3667 cluster with the following results.

Name	Method	Field strength (μG)	Location
Coma	Equipartition	0.45	radio halo
	Equipartition	0.55	radio relic
	Faraday Rotation	7	cluster center
	Faraday Rotation	0.2	cluster center(large scale)
	Inverse Compton	0.2	cluster average
A3667	Equipartition	1.5−2.5	NW relic
	Inverse Compton	≥ 0.4	cluster average
	Faraday Rotation	1−2	cluster center
	Faraday Rotation	3−5	NW relic
	Cold front	10	along the cold fronts

Figure 4.21: Possible values that can be obtained through various methods applied to the Coma and A3367 cluster (Carilli 2002).

If we make a direct comparison of the values for other clusters with what we have found, we can see that 25 μG seems out of line even for the high values with RM and cold fronts. In this research we have used the values presented in sec. 4.3.1 along with 15 μG as a middle-ground value. Further analysis on the Perseus cluster with

different methods (synchrotron, IC,...) will help determining the exact value, but we expect values more in line with what shown fig. 4.20. Inverse Compton may show a much weaker field which can be explained by making some assumptions about the electron energy spectrum and pitch-angle distribution (Carilli and Taylor 2002):

- An anisotropic pitch-angle distribution biased toward low angles would clearly weaken the radio synchrotron radiation relative to the IC X-ray emission. Such a distribution will occur naturally given that electrons at large pitch angles have greater synchrotron losses.
- The IC hard X-ray emission is from relativistic electrons with $\gamma \sim 5000$. This corresponds to radio continuum emission at 100 MHz for μG magnetic fields. Most surveys of cluster radio halos have been done at 1.4 (Govoni 2018), corresponding to electron Lorentz factors of $\gamma \sim 18000$. A steepening in the electron energy spectrum at Lorentz factors around 10^4 will reduce the 1.4 GHz radio luminosities, but retain the IC hard X-ray emission.
- Magnetic substructure, or filamentation, can lead to a significant difference between fields estimated using the different techniques.

Following this, we have implemented these values in the various possible profiles for the magnetic field in the cluster and we have confronted them with a few observations that have been made so far. With the data obtained in sections 4.3.2 and 4.3.2, we can make an argument for establishing lower limit of the magnetic field at 1 μG. With what discussed in 4.3.2, the explanation for the discrepancy between IC-(B $>$ 1 μG) and ϕ-(B $>$ 0.12 $\pm$ 0.01 or B $>$ 0.019 $\pm$ 0.01) derived magnetic fields is to assume that the hard X-rays are not IC in origin. The Faraday depth could place a higher lower boundary but the error expected on it is probably much higher than what calculations show, since it depends on the electron density and the possible length of the cloud in front of it. We should mention that the position and structure of IC310 may complicate precise evaluations of the magnetic field. Fig. 4.25 shows a the structure for the Perseus cluster further proven by Fig. 4.26, the situation in IC310 and in the nearby regions may be more complicated than expected as drops in temperature are presented both in the center and in the outer regions. This lower limit would exclude most of the possible models obtained, but it also helps to establish a better range of values for the central magnetic field. Fig. 4.12, 4.13, 4.14, 4.15, 4.16, 4.17, show a steep drop in values at the variation of η. We can make an argument on why some of this models are not consistent with the few data in our possession. $\eta = 0.9$ may be to steep as it has been proven as the correct value for cluster A119, where the polarization properties of 3 extended radio galaxies have been studied, this could be an exception, not a general rule.This model predicts a drastic drop in the B-field intensity as the radii increases, this model is never consistent with the observations. Also $\eta = \frac{2}{3}$, may be a too rough of an approximation for this model as it considers only the magnetic flux conservation, but still, it cannot be excluded completely as some cases are consistent with the observations (Govoni 2018). As shown in the data the model with $\eta = 0.5$ seems the most consistent with the observations. The models made trough turbulence behaviour of the ICM show to be mostly inconsistent, but this can be explained by the fact that in addition to the electron density uncertainty, there is an additional uncertainty brought by the distribution of galaxies which may create large underestimations of the error. Further methods of analysis should be implemented to narrow down the range of values for both NGC1275 and IC310.

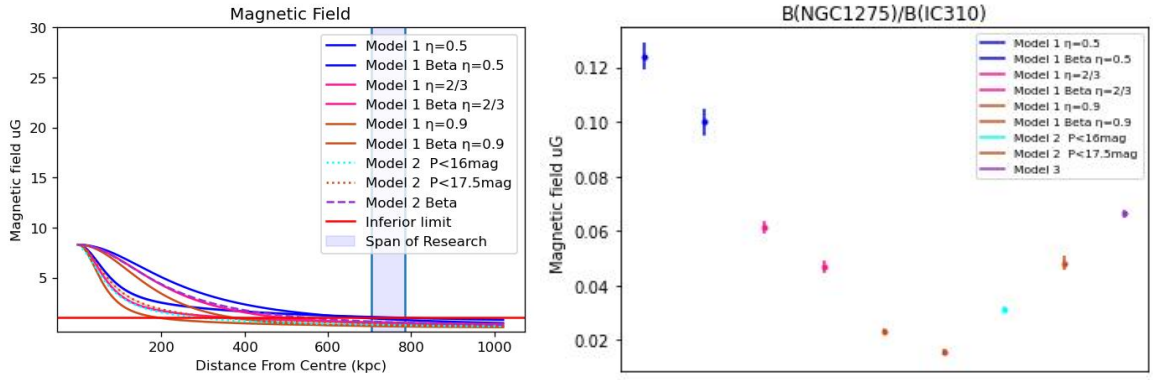

Figure 4.22: Plots of the various models obtained with the central magnetic field strength of 8.3 μG (on the left), plot of the ratio between the central magnetic field strength (8.3 μG) and the magnetic field strength at the position of IC310 (on the rigth)

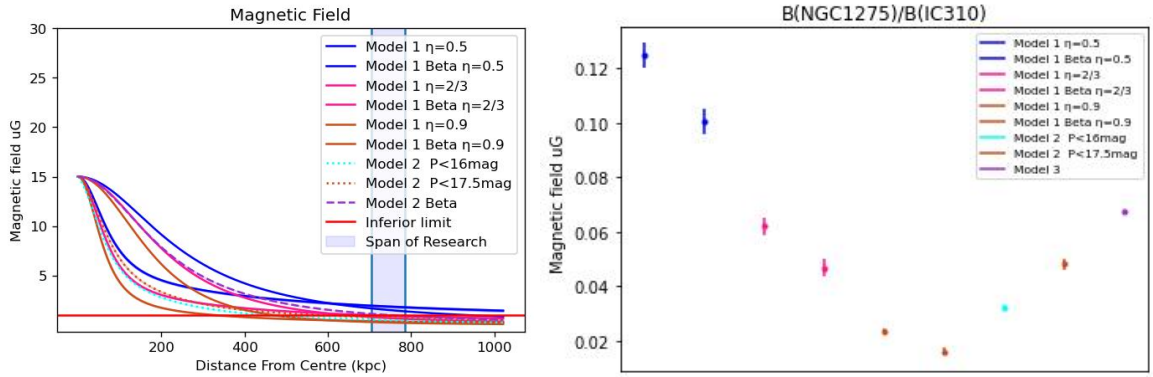

Figure 4.23: Plots of the various models obtained with the central magnetic field strength of 15 μG (on the left), plot of the ratio between the central magnetic field strength (15 μG) and the magnetic field strength at the position of IC310 (on the rigth)

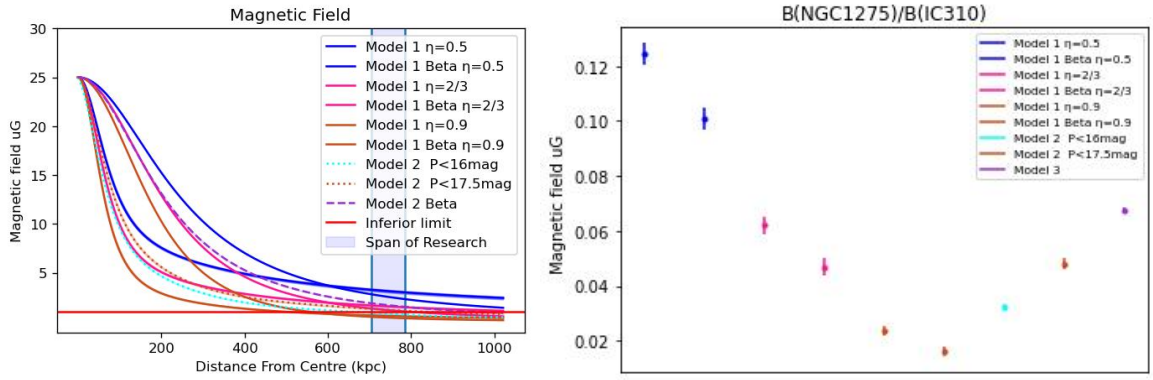

Figure 4.24: Plots of the various models obtained with the central magnetic field strength of 25 μG (on the left), plot of the ratio between the central magnetic field strength (25 μG) and the magnetic field strength at the position of IC310 (on the rigth)

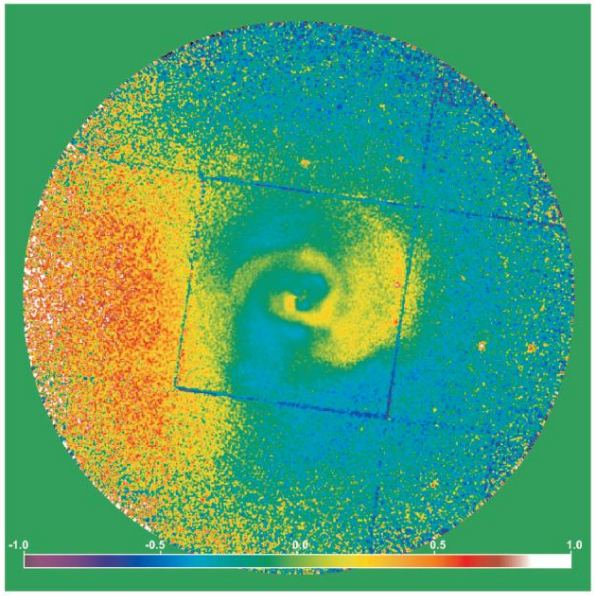

Figure 4.25: The relative deviation of the surface brightness from the azimuthally averaged value of the Perseus Cluster (Churazov et al. 2003).

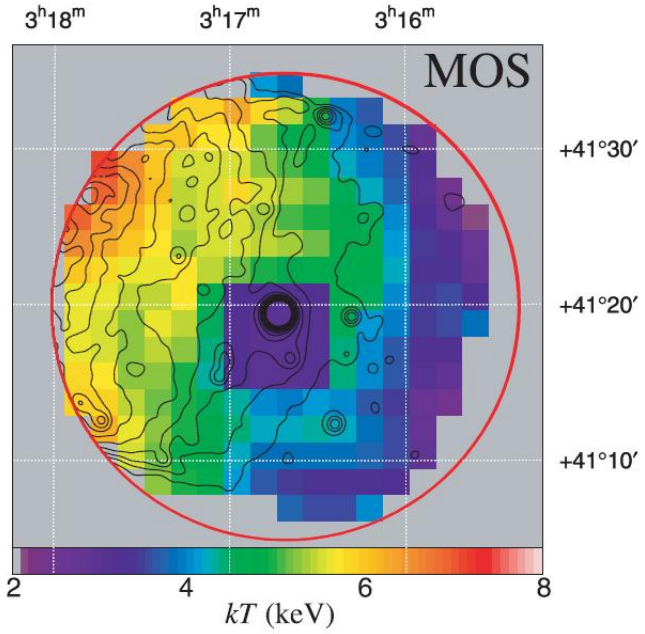

Figure 4.26: Temperature maps of IC310 obtained by MOS (Sato et al. 2005).

5. Conclusion and Outlook

In this work, we have studied the magnetic fields in clusters of galaxies, in collaboration with the MAGIC project, in particular we have focused our efforts on the Perseus Cluster by studying the magnetic field strength in the IC310 galaxy and trying to extablish a relation with the central magnetic field value. This study, other than to improve our general understanding in magnetic fields in GCs, can be implemented in other research fields, in particular the research of ALPs. Literature on the subject was briefly summed up, then it was applied to the Perseus Cluster. We have established some possible models by looking at the distribution of the ICM in various methods and the distributions of the galaxies in the cluster in various methods. Plotting this models with the central field values given (Libanov and Troitsky 2020; Taylor et al. 2006), permitted us to have a general idea on the magnetic field profile and establish some theorethical values for the magnetic field strength at the position of IC310. By looking at the available data for IC310 we have lower limit for the magnetic field strength of $B > 1$ μG (Sato et al. 2005). After this lower limit was implemented in our reasoning some of the models initially hypothesized were discarded, but the range of research of 8.3-25 μG as the central magnetic field was deemed appropriate. Further research should focus on improving our knowledge on the distribution of the electronic gas in the cluster, study of the radio emission of the cluster could help this. The morphology of the cluster should also be better studied as the data used for the distribution of galaxies in the cluster is probably obsolete (Bahcall 1974) by the modern standards of research. There should be also an attempt to study the dynamical conditions of IC310 and nearby areas, a confirmation of the presence of a cold front could place a higher constraint on the magnetic field at the position of IC310 and in direct conseguence of that a higher lower limit of the central magnetic field strength. This range of the magnetic field strength value could be a good starting point for the research of ALPs by using the Perseus cluster as source of γ-rays, MAGIC telescopes are the best option to search, because their sensitivities are higher and their energy ranges are bigger than other CTAs. After observations have been made softwares like gammapy should be used to find possible imprints on the spectra of astrophysical sources of ALPs (sec. 3).

Bibliography

Ahnen, M.L. et al. (2017). *Performance of the MAGIC telescope under moonlight*. arXiv:1704.00906v4: Astroparticle Physics.

Aleksi'c, J. et al. (Mar. 2014). "Rapid and multiband variability of the TeV bright active nucleus of the galaxy IC 310". In: *aap* 563, A91, A91. DOI: 10.1051/0004-6361/201321938. arXiv: 1305.5147 [astro-ph.HE].

Angelis, Alessandro De, Marco Roncadelli, and Oriana Mansutti (Dec. 2007). "Evidence for a new light spin-zero boson from cosmological gamma-ray propagation?" In: *Physical Review D* 76.12. DOI: 10.1103/physrevd.76.121301. URL: https://doi.org/10.1103%2Fphysrevd.76.121301.

Arias, Paola et al. (June 2012). "WISPy cold dark matter". In: *Journal of Cosmology and Astroparticle Physics* 2012.06, pp. 013–013. DOI: 10.1088/1475-7516/2012/06/013. URL: https://doi.org/10.1088%2F1475-7516%2F2012%2F06%2F013.

Arnaud, M. (2009). "The el of the intracluster medium - Commentary on: Cavaliere A. and Fusco-Femiano R., 1976, A&A, 49, 137". In: *A&A* 500.1, pp. 103–104. DOI: 10.1051/0004-6361/200912150. URL: https://doi.org/10.1051/0004-6361/200912150.

Bahcall, N. A. (Feb. 1974). "The Perseus Cluster: Galaxy Distribution, Anisotropy, and the Mass/luminosity Ratio". In: *apj* 187, pp. 439–444. DOI: 10.1086/152651.

Batković, Ivana et al. (June 2021). "Axion-like Particle Searches with IACTs". In: *Universe* 7.6, p. 185. DOI: 10.3390/universe7060185. URL: https://doi.org/10.3390%2Funiverse7060185.

Beck R., et al. (1996). *Galactic Magnetism: Recent Developments and Perspectives*. Vol. 34. Annual Review of Astronomy and Astrophysics, pp. 155–206.

Bouvier, A. (2011). *Prospects of GRB observation for CTA from a phenomenological model*. arXiv:1109.5680v1: ResearchGate.

Brentjens, M. A. and A. G. de Bruyn (Sept. 2005). "Faraday rotation measure synthesis". In: *Astronomy & Astrophysics* 441.3, pp. 1217–1228. DOI: 10.1051/0004-6361:20052990. URL: https://doi.org/10.1051%2F0004-6361%3A20052990.

— (2006). "RM-synthesis of the Perseus cluster". In: *Astronomische Nachrichten* 327.5-6, pp. 545–548. DOI: https://doi.org/10.1002/asna.200610584. eprint: https://onlinelibrary.wiley.com/doi/pdf/10.1002/asna.200610584. URL: https://onlinelibrary.wiley.com/doi/abs/10.1002/asna.200610584.

Bridle, Alan H. (1984). *Extragalactic Radio Jets*. Vol. 22. Annual Review of Astronomy and Astrophysics, pp. 319–358.

Brunetti G., et al.. (2001). *Monthly notices of the Royal Astronomical Journal 320*.

Bruyn, A. G. de and M. A. Brentjens (2005). "Diffuse polarized emission associated with the Perseus cluster". In: *A&A* 441.3, pp. 931–947. DOI: 10.1051/0004-6361:20052992. URL: https://doi.org/10.1051/0004-6361:20052992.

Burn, B. J. (1966). *Monthly notices of the Royal Astronomical Journal 133*.

Carilli, C. L. (2002). *Cluster Magnetic Fields*.

Carilli, C. L. and G. B. Taylor (Sept. 2002). “Cluster Magnetic Fields”. In: *Annual Review of Astronomy and Astrophysics* 40.1, pp. 319–348. DOI: 10.1146/annurev.astro.40.060401.093852. URL: https://doi.org/10.1146%2Fannurev.astro.40.060401.093852.

Chandran, B. D. G. and S. C. Cowley (1998). *Physical Review Letters*.

Churazov, E. et al. (June 2003). “XMM-Newton Observations of the Perseus Cluster. I. The Temperature and Surface Brightness Structure”. In: *The Astrophysical Journal* 590.1, pp. 225–237. DOI: 10.1086/374923. URL: https://doi.org/10.1086%2F374923.

De Angelis, A. et al. (Mar. 2009). “Photon propagation and the very high energy γ-ray spectra of blazars: how transparent is the Universe?” In: *Monthly Notices of the Royal Astronomical Society: Letters* 394.1, pp. L21–L25. ISSN: 1745-3925. DOI: 10.1111/j.1745-3933.2008.00602.x. eprint: https://academic.oup.com/mnrasl/article-pdf/394/1/L21/3779643/394-1-L21.pdf. URL: https://doi.org/10.1111/j.1745-3933.2008.00602.x.

De Angelis, Alessandro, Giorgio Galanti, and Marco Roncadelli (Nov. 2011). “Relevance of axion-like particles for very-high-energy astrophysics”. In: *Phys. Rev. D* 84 (10), p. 105030. DOI: 10.1103/PhysRevD.84.105030. URL: https://link.aps.org/doi/10.1103/PhysRevD.84.105030.

Dine, Michael, Willy Fischler, and Mark Srednicki (1981). “A simple solution to the strong CP problem with a harmless axion”. In: *Physics Letters B* 104.3, pp. 199–202. ISSN: 0370-2693. DOI: https://doi.org/10.1016/0370-2693(81)90590-6. URL: https://www.sciencedirect.com/science/article/pii/0370269381905906.

Dolag, K., M. Bartelmann, and H. Lesch (2002). “Evolution and structure of magnetic fields in simulated galaxy clusters”. In: *A&A* 387.2, pp. 383–395. DOI: 10.1051/0004-6361:20020241. URL: https://doi.org/10.1051/0004-6361:20020241.

Dolag, K., S. Schindler, et al. (2001). “Correlation of the magnetic field and the intra-cluster gas density in galaxy clusters”. In: *A&A* 378.3, pp. 777–786. DOI: 10.1051/0004-6361:20011219. URL: https://doi.org/10.1051/0004-6361:20011219.

Dolag, Klaus, Matthias Bartelmann, and Harald Lesch (2002). “Evolution and structure of magnetic fields in simulated galaxy clusters”. In: DOI: 10.48550/ARXIV.ASTRO-PH/0202272. URL: https://arxiv.org/abs/astro-ph/0202272.

Feretti, L. et al. (Apr. 1999). “The radio galaxies and the magnetic field in Abell 119”. In: *aap* 344, pp. 472–482. arXiv: astro-ph/9902019 [astro-ph].

Giovannini, G. et al. (Apr. 1993). “The Halo Radio Source Coma C and the Origin of Halo Sources”. In: *apj* 406, p. 399. DOI: 10.1086/172451.

Gourgouliatos, Konstantinos Nektarios, Jonathan Braithwaite, and Maxim Lyutikov (Oct. 2010). “Structure of magnetic fields in intracluster cavities”. In: *Monthly Notices of the Royal Astronomical Society* 409.4, pp. 1660–1668. DOI: 10.1111/j.1365-2966.2010.17410.x. URL: https://doi.org/10.1111%2Fj.1365-2966.2010.17410.x.

Govoni, F. Luigina Feretti (2018). *Magnetic Fields in Clusters of Galaxies*.

Hanisch, R.J. (Dec. 1970). “A search for radio halo emission at 430 MHz in 72 rich clusters of galaxies”. In: *Astronomy and Astrophysics* 1. URL: https://adsabs.harvard.edu/full/1982A%26A...111...97H.

Harris, D. E., V. K. Kapahi, and R. D. Ekers (Feb. 1980). “Westerbork synthesis observations of 8 clusters of galaxies which contain tailed radio galaxies.” In: *aaps* 39, pp. 215–233.

Hildebrand, Dorothée Maria (2012). “Detection of very high energy γ-ray emission from active galactic nuclei in the central region of the perseus cluster”. In: DOI: https://doi.org/10.3929/ethz-a-007342444.

Hooper, Dan and Pasquale D. Serpico (Dec. 2007). “Detecting Axion-like Particles with Gamma Ray Telescopes”. In: *Physical Review Letters* 99.23. DOI: 10.1103/physrevlett.99.231102. URL: https://doi.org/10.1103%2Fphysrevlett.99.231102.

Horns, Dieter et al. (Oct. 2012). “Hardening of TeV gamma spectrum of active galactic nuclei in galaxy clusters by conversions of photons into axionlike particles”. In: *Phys. Rev. D* 86 (7), p. 075024. DOI: 10.1103/PhysRevD.86.075024. URL: https://link.aps.org/doi/10.1103/PhysRevD.86.075024.

Jaeckel, J. A. Ringwald (2010). *The Low-Energy Frontier of Particle Physics*. Vol. 60. Annual Review of Nuclear and Particle Science, p. 405. DOI: 10.1146/annurev.nucl.012809.104433.

Jaffe, W. (1980). *On The Morphology Of The Magnetic Field In Galaxy Cluster*.

Kim, Jihn E. (July 1979). “Weak-Interaction Singlet and Strong CP-Invariance”. In: *Phys. Rev. Lett.* 43 (2), pp. 103–107. DOI: 10.1103/PhysRevLett.43.103. URL: https://link.aps.org/doi/10.1103/PhysRevLett.43.103.

Kulsrud, Russel M. (1999). *A Critical Review of Galactic Dynamos*. Vol. 37. Annual Review of Astronomy and Astrophysics, pp. 37–64.

Large, M. (June 1959). “A High-Resolution Survey of the Coma Cluster of Galaxies at 408 Mc./s.” In: *Nature* 83. DOI: https://doi.org/10.1038/1831663a0. URL: https://www.nature.com/articles/1831663a0#citeas.

Libanov, Maxim and Sergey Troitsky (2020). “On the impact of magnetic-field models in galaxy clusters on constraints on axion-like particles from the lack of irregularities in high-energy spectra of astrophysical sources”. In: *Phys. Lett. B* 802, p. 135252. DOI: 10.1016/j.physletb.2020.135252. arXiv: 1908.03084 [astro-ph.HE].

Markevitch, M. et al. (Oct. 2000). “Chandra Observation of Abell 2142: Survival of Dense Subcluster Cores in a Merger”. In: *apj* 541.2, pp. 542–549. DOI: 10.1086/309470. arXiv: astro-ph/0001269 [astro-ph].

Marsh, M.C. David et al. (Dec. 2017). “A new bound on axion-like particles”. In: *Journal of Cosmology and Astroparticle Physics* 2017.12, pp. 036–036. DOI: 10.1088/1475-7516/2017/12/036. URL: https://doi.org/10.1088%2F1475-7516%2F2017%2F12%2F036.

Meyer, Manuel, Dieter Horns, and Martin Raue (Feb. 2013). “First lower limits on the photon-axion-like particle coupling from very high energy gamma-ray observations”. In: *Physical Review D* 87.3. DOI: 10.1103/physrevd.87.035027. URL: https://doi.org/10.1103%2Fphysrevd.87.035027.

Miley, G. (Jan. 1980). “The structure of extended extragalactic radio sources”. In: *araa* 18, pp. 165–218. DOI: 10.1146/annurev.aa.18.090180.001121.

Mirizzi, Alessandro and Daniele Montanino (Jan. 2017). “Stochastic conversions of TeV photons into axion-like particles in extragalactic magnetic fields”. In: *Journal of Cosmology and Astroparticle Physics* 2009.12,

pp. 004–004. DOI: 10.1088/1475-7516/2009/12/004. URL: https://doi.org/10.1088%2F1475-7516%2F2009%2F12%2F004.

Neronov, A., D. Semikoz, and Ie. Vovk (Sept. 2010). "Very high-energy γ-ray emission from IC310". In: *Astronomy and Astrophysics* 519, p. L6. DOI: 10.1051/0004-6361/201014499. URL: https://doi.org/10.1051%2F0004-6361%2F201014499.

Parker, E. N. (1979). *Cosmical magnetic fields. Their origin and their activity*. The International Series of Monographs on Physics , Oxford: Clarendon Press. ISBN: 978-0198829966.

Perkins, J. S. et al. (June 2006). "TeV Gamma-Ray Observations of the Perseus and Abell 2029 Galaxy Clusters". In: *The Astrophysical Journal* 644.1, pp. 148–154. DOI: 10.1086/503321. URL: https://doi.org/10.1086/503321.

Quinn (June 1977). "CP-Conservation in the Presence of Pseudoparticles". In: *Phys. Rev. Lett.* 38 (25), pp. 1440–1443. DOI: 10.1103/PhysRevLett.38.1440. URL: https://link.aps.org/doi/10.1103/PhysRevLett.38.1440.

Raffelt, Georg and Leo Stodolsky (Mar. 1988). "Mixing of the photon with low-mass particles". In: *Phys. Rev. D* 37 (5), pp. 1237–1249. DOI: 10.1103/PhysRevD.37.1237. URL: https://link.aps.org/doi/10.1103/PhysRevD.37.1237.

Sá nchez-Conde, M. A. et al. (June 2009). "Hints of the existence of axion-like particles from the gamma-ray spectra of cosmological sources". In: *Physical Review D* 79.12. DOI: 10.1103/physrevd.79.123511. URL: https://doi.org/10.1103%2Fphysrevd.79.123511.

Sanders, J. S., A. C. Fabian, and R. J. H. Dunn (June 2005). "Non-thermal X-rays, a high-abundance ridge and fossil bubbles in the core of the Perseus cluster of galaxies". In: *Monthly Notices of the Royal Astronomical Society* 360.1, pp. 133–140. DOI: 10.1111/j.1365-2966.2005.09016.x. URL: https://doi.org/10.1111%2Fj.1365-2966.2005.09016.x.

Sato, K. et al. (Oct. 2005). "XMM-Newton Observation of IC 310 in the Outer Region of the Perseus Cluster of Galaxies". In: *Publications of the Astronomical Society of Japan* 57.5, pp. 743–749. DOI: 10.1093/pasj/57.5.743. URL: https://doi.org/10.1093%2Fpasj%2F57.5.743.

Schmidt, R. W., A. C. Fabian, and J. S. Sanders (Nov. 2002). "Chandra temperature and metallicity maps of the Perseus cluster core". In: *Monthly Notices of the Royal Astronomical Society* 337.1, pp. 71–78. DOI: 10.1046/j.1365-8711.2002.05804.x. URL: https://doi.org/10.1046%2Fj.1365-8711.2002.05804.x.

Soward, A. M. (1983). *Stellar and Planetary Magnetism (The Fluid Mechanics of Astrophysics and Geophysics)*. Vol. 2. Gordon and Breach Science Publishers. ISBN: 978-0677164304.

Spitzer, L. (1978). *Physical Processes in the Interstellar Medium*. New York:Wiley. ISBN: 978-0471293354.

— (1956). *Physics of Fully Ionized Gases*.

Taylor, G. B. et al. (June 2006). "Magnetic fields in the centre of the Perseus cluster". In: *Monthly Notices of the Royal Astronomical Society* 368.4, pp. 1500–1506. DOI: 10.1111/j.1365-2966.2006.10244.x. URL: https://doi.org/10.1111%2Fj.1365-2966.2006.10244.x.

Vikhlinin, A. et al (2001). *Astrophysical Journal*.

Westfold, K.C. (1959). *Astrophysical Journal 130*.

Willson, M. (Dec. 1970). “Radio Observations of the Cluster of Galaxies in Coma Berenices—the 5C4 Survey”. In: *Monthly Notices of the Royal Astronomical Society* 151. DOI: https://doi.org/10.1093/mnras/151.1.1. URL: https://academic.oup.com/mnras/article/151/1/1/2888660.

Yamasaki, N. Y., T. Ohashi, and T. Furusho (Oct. 2002). “Chandra Observation of the Central Galaxies in the A1060 Cluster of Galaxies”. In: *The Astrophysical Journal* 578.2, pp. 833–841. DOI: 10.1086/342652. URL: https://doi.org/10.1086%2F342652.